

UNCLASSIFIED

AD NUMBER
ADB274597
NEW LIMITATION CHANGE
TO Approved for public release, distribution unlimited
FROM Distribution authorized to U.S. Gov't. agencies only; Proprietary Info.; Oct 2001. Other requests shall be referred to U.S. Army Medical Research and Materiel Command, 504 Scott St., Ft. Detrick, MD 21702-5012.
AUTHORITY
USAMRMC ltr, 28 Aug 2002

THIS PAGE IS UNCLASSIFIED

AD _____

Award Number: DAMD17-00-1-0650

TITLE: Molecular Diffuse Optical Tomography for Early Breast Cancer Detection and Characterization

PRINCIPAL INVESTIGATOR: Vasilis Ntziachristos, Ph.D.

CONTRACTING ORGANIZATION: Massachusetts General Hospital
Boston, Massachusetts 02114-2554

REPORT DATE: October 2001

TYPE OF REPORT: Final

PREPARED FOR: U.S. Army Medical Research and Materiel Command
Fort Detrick, Maryland 21702-5012

DISTRIBUTION STATEMENT: Distribution authorized to U.S. Government agencies only (proprietary information, Oct 01). Other requests for this document shall be referred to U.S. Army Medical Research and Materiel Command, 504 Scott Street, Fort Detrick, Maryland 21702-5012.

The views, opinions and/or findings contained in this report are those of the author(s) and should not be construed as an official Department of the Army position, policy or decision unless so designated by other documentation.

20020118 112

NOTICE

USING GOVERNMENT DRAWINGS, SPECIFICATIONS, OR OTHER DATA INCLUDED IN THIS DOCUMENT FOR ANY PURPOSE OTHER THAN GOVERNMENT PROCUREMENT DOES NOT IN ANY WAY OBLIGATE THE U.S. GOVERNMENT. THE FACT THAT THE GOVERNMENT FORMULATED OR SUPPLIED THE DRAWINGS, SPECIFICATIONS, OR OTHER DATA DOES NOT LICENSE THE HOLDER OR ANY OTHER PERSON OR CORPORATION; OR CONVEY ANY RIGHTS OR PERMISSION TO MANUFACTURE, USE, OR SELL ANY PATENTED INVENTION THAT MAY RELATE TO THEM.

LIMITED RIGHTS LEGEND

Award Number: DAMD17-00-1-0650
Organization: Massachusetts General Hospital

Those portions of the technical data contained in this report marked as limited rights data shall not, without the written permission of the above contractor, be (a) released or disclosed outside the government, (b) used by the Government for manufacture or, in the case of computer software documentation, for preparing the same or similar computer software, or (c) used by a party other than the Government, except that the Government may release or disclose technical data to persons outside the Government, or permit the use of technical data by such persons, if (i) such release, disclosure, or use is necessary for emergency repair or overhaul or (ii) is a release or disclosure of technical data (other than detailed manufacturing or process data) to, or use of such data by, a foreign government that is in the interest of the Government and is required for evaluational or informational purposes, provided in either case that such release, disclosure or use is made subject to a prohibition that the person to whom the data is released or disclosed may not further use, release or disclose such data, and the contractor or subcontractor or subcontractor asserting the restriction is notified of such release, disclosure or use. This legend, together with the indications of the portions of this data which are subject to such limitations, shall be included on any reproduction hereof which includes any part of the portions subject to such limitations.

THIS TECHNICAL REPORT HAS BEEN REVIEWED AND IS APPROVED FOR PUBLICATION.

Kath Mome 12/28/01

REPORT DOCUMENTATION PAGEForm Approved
OMB No. 074-0188

Public reporting burden for this collection of information is estimated to average 1 hour per response, including the time for reviewing instructions, searching existing data sources, gathering and maintaining the data needed, and completing and reviewing this collection of information. Send comments regarding this burden estimate or any other aspect of this collection of information, including suggestions for reducing this burden to Washington Headquarters Services, Directorate for Information Operations and Reports, 1215 Jefferson Davis Highway, Suite 1204, Arlington, VA 22202-4302, and to the Office of Management and Budget, Paperwork Reduction Project (0704-0188), Washington, DC 20503

1. AGENCY USE ONLY (Leave blank)**2. REPORT DATE**

October 2001

3. REPORT TYPE AND DATES COVERED

Final (1 Oct 00 - 30 Sep 01)

4. TITLE AND SUBTITLE

Molecular Diffuse Optical Tomography for Early Breast Cancer Detection and Characterization

5. FUNDING NUMBERS

DAMD17-00-1-0650

6. AUTHOR(S)

Vasilis Ntziachristos, Ph.D.

7. PERFORMING ORGANIZATION NAME(S) AND ADDRESS(ES)Massachusetts General Hospital
Boston, Massachusetts 02114-2554E-mail: vasilis@helix.mgh.harvard.edu**8. PERFORMING ORGANIZATION
REPORT NUMBER****9. SPONSORING / MONITORING AGENCY NAME(S) AND ADDRESS(ES)**U.S. Army Medical Research and Materiel Command
Fort Detrick, Maryland 21702-5012**10. SPONSORING / MONITORING
AGENCY REPORT NUMBER****11. SUPPLEMENTARY NOTES****12a. DISTRIBUTION / AVAILABILITY STATEMENT**

Distribution authorized to U.S. Government agencies only (proprietary information, Oct 01). Other requests for this document shall be referred to U.S. Army Medical Research and Materiel Command, 504 Scott Street, Fort Detrick, Maryland 21702-5012.

12b. DISTRIBUTION CODE**13. ABSTRACT (Maximum 200 Words)**

Herein we demonstrate the construction of the first reported fluorescence animal tomographer for molecular investigations of cancer-associated expression patterns. Using inversion techniques that account for the diffuse nature of photon propagation in tissue and near infrared fluorescent molecular beacons we were able to obtain three-dimensional in-vivo images of cathepsin B expression of orthopic gliomas. We demonstrate that fluorescent probes, activated by carcinogenesis, can be detected with high positional accuracy and high sensitivity in deep tissues, that molecular specificities of different beacons towards enzymes can be resolved, and that tomography of beacon activation is linearly related to enzyme concentration. The tomographic imaging method offers a range of new capabilities for studying biological function using fluorescent chemical sensors, for identifying molecular expression patterns via multispectral imaging and for continuously monitoring drug therapies. It is envisaged that molecular sensing will significantly improve the detection capacity of early cancer since malignancy identification is based on the molecular signals responsible for carcinogenesis and not on structural or functional tissue changes inflicted by well-formed cancers that are currently targeted by traditional medical imaging techniques.

14. SUBJECT TERMS

Molecular Imaging, Fluorescence, Tomography

15. NUMBER OF PAGES

48

16. PRICE CODE**17. SECURITY CLASSIFICATION
OF REPORT**

Unclassified

**18. SECURITY CLASSIFICATION
OF THIS PAGE**

Unclassified

**19. SECURITY CLASSIFICATION
OF ABSTRACT**

Unclassified

20. LIMITATION OF ABSTRACT

Unlimited

Table of Contents

Cover.....	
SF 298.....	2
Table of Contents.....	3
Introduction.....	4
Body.....	4
Key Research Accomplishments.....	12
Reportable Outcomes.....	12
Conclusions.....	12
References.....	13
Appendices.....	14

Introduction

There exists a need for innovative research to develop new imaging technologies for sensing and quantitating molecular signatures in vivo and in deep tissues^{1,2}. The main rationale for developing such technologies is 2-fold: a) to allow the earlier detection of disease based on molecular abnormalities and b) gain a better understanding of disease mechanisms to allow efficient targeting of specific signatures for early detection and for treatment. The non-invasive three-dimensional mapping and quantification of cellular and sub-cellular events in living organisms, represents a highly novel and unexplored field in imaging sciences that is expected to have a major impact in biomedical research and the clinical practice of diagnostic imaging. The development of novel optical tomographic techniques and molecular fluorescent probes in the NIR can significantly enhance molecular and cell biology techniques, in the in-vivo study of cancers in deep tissues. Technologies that use light have been developed in the past to target oxy- and deoxy-hemoglobin or vascular contrast agents. Under this concept award we investigated whether this technology, after necessary improvements and modifications, would be adequate to sense, reconstruct and quantify fluorescent reporters from within tissues in-vivo and in a non-invasive manner. Fluorescence-mediated molecular tomography (FMT) is a sensitive imaging modality that reconstructs and quantifies the distribution of fluorescent reporters within tissue with high sensitivity. The specific reporters targeted were activatable near-infrared probes that are non-fluorescing in their native state but are activated in the presence of specific enzymes that are over-expressed in carcinomas³. For imaging purposes, we developed a highly sensitive imager with three-dimensional imaging capabilities, able to detect signals at both intrinsic and fluorescent wavelengths⁴. We further developed the necessary algorithms for very accurate reconstructions, adapted specifically to the requirements of imaging living tissue⁴. We tested the technology with phantoms and subsequently applied it in-vivo imaging of animal models. The importance of this imaging strategy is further amplified by considering that one of the major drawbacks of CT and MRI contrast agents has been the need to deliver them at μ molar tissue concentrations. Similar to nuclear imaging, photon technology detection has superior sensitivity detecting fluorescent molecules at nano- to picomolar concentrations. One significant advantage of fluorescent molecules over isotopes is that they can be quenched and de-quenched, enabling the design of molecular switches or 'beacons'. A further benefit is the use of non-ionizing radiation and the relatively low cost instrumentation required.

Body

Imaging molecular targets in vivo

The goal of the research performed lies in the development of new sets of strategies to interrogate targets at subcellular levels (Fig. 1). These targets are ultimately responsible for pathogenesis and represent the key points for targeting early detection and subsequent therapeutic intervention. The impact of developing molecular imaging techniques is potentially enormous. First, relatively crude parameters of tumor growth and development (tumor burden, anatomic location etc.) could be supplemented by more specific parameters (e.g. growth factor receptors, cell surface markers, transduction signals, cell cycle proteins etc.). Second, this added information is expected to go hand-

in-hand with the development of novel targeted detection strategies that will allow us to assess tumors at a molecular level, long before phenotypic changes occur. This, in turn, is expected to have an impact in the level of specificity in detecting not only the tumor presence but its molecular synthesis and further initiating appropriate targeted treatment in case of malignancy. Third, molecular imaging potentially allows one to study the genesis of diseases in the intact microenvironment of living systems, which is currently very difficult to do otherwise. The importance of intact micro- and macroenvironments on tumor progression has recently been recognized⁵⁻⁷. Fourth, molecular imaging will be critical in testing novel drug delivery strategies as there exist significant barriers to the delivery of complex and molecular therapies⁵. Understanding these barriers and finding solutions to modulate them will be of utmost importance in future drug development. Finally, molecular imaging allows one to gain three-dimensional information that may be much faster to obtain than is currently possible with time consuming and labor intensive conventional technique. The key elements to sampling molecular information are summarized in Fig. 1. We believe that FMT imaging with activatable "smart" imaging probes will become a key enabling technology towards the above goals.

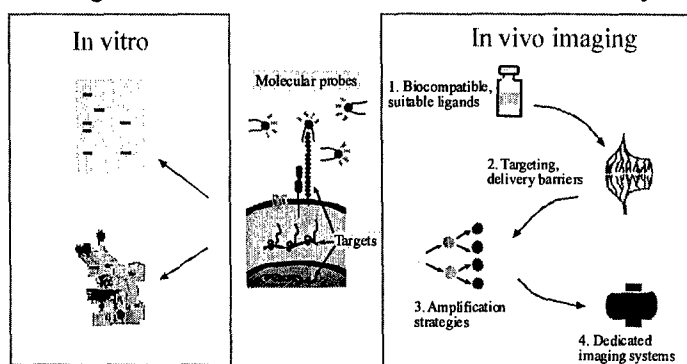


Fig 1: Comparison of *in vitro* and *in vivo* molecular imaging.

"Smart" imaging probes

Photon detection has high intrinsic sensitivity allowing the detection of fluorescent molecules at pico- to femtomolar concentrations (see appendix), similar to isotope concentrations in nuclear medicine. One significant advantage of fluorescent molecules over isotopes is that they can be quenched and de-quenched, enabling the design of molecular switches or 'beacons'. The underpinning mechanism of action of the previously conceived molecular probes is illustrated in Fig. 2. The probes are essentially non-fluorescent in their native (quenched) state and become highly fluorescent after target interaction, resulting in signal amplification of up to several hundred-fold, depending on the specific design. This approach has four major advantages over other methods when single fluorochromes are attached to affinity molecules: 1) a single enzyme can cleave multiple fluorochromes, thus resulting in one form of signal amplification, 2) reduction of background "noise" by several orders of magnitude is possible, 3) very specific enzyme activities can potentially be interrogated and 4) multiple probes can be arranged on delivery systems to simultaneously probe for a spectrum of enzymes.

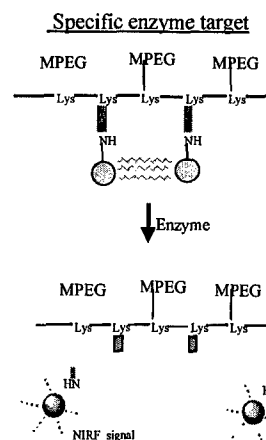


Fig. 2: Example of activatable enzyme specific imaging probes. Note that the fluorochromes are excited in the near infrared.

A number of different designs of optical smart agents have been described. In this work we employed a probe designed to report on specific enzyme activities. The probes typically consist of three building blocks: 1) near infrared fluorochromes, 2) peptide substrates and 3) a delivery vehicle. The design of the probes has been described in detail elsewhere³ and basically uses certain peptide substrates (Table 2) attached to a delivery molecule to impart molecular specificity. When a given target protease cleaves the substrate, the fluorochromes are released (see Fig.2) and fluorescence is emitted (de-quenching). Specific examples are tumor lysosomal endopeptidases that recognize and cleave free lysine residues (cathepsin B)⁸, cathepsin D which cleaves two phenylalanine peptides⁹, MMP-2 specific probes¹⁰ or caspase-3 specific probes.

Table 2: Peptide substrates synthesized in our lab (The dots indicate the cleavage site)

Protease target	Peptide sequence
Cathepsin B	GRR•G
Cathepsin D	GPIC(Et)F•FRLG
Matrix metalloproteinase 2	GPLG•VRG
Caspase 3	DEVD•G
Prostate specific antigen	HSSKLQ•G

Prototype FMT imaging system

According to the original statement of work a prototype fluorescence-mediated molecular tomography system for 3D quantitative imaging in mice was build. The system components and reconstruction algorithm were specifically chosen and/or developed to a) detect fluorescence activation in vivo (i.e. record the smart probes), b) be quantitative and c) be adaptable to larger scales or different geometries. The following is a description of the system components while subsequent paragraphs detail the experimental results obtained.

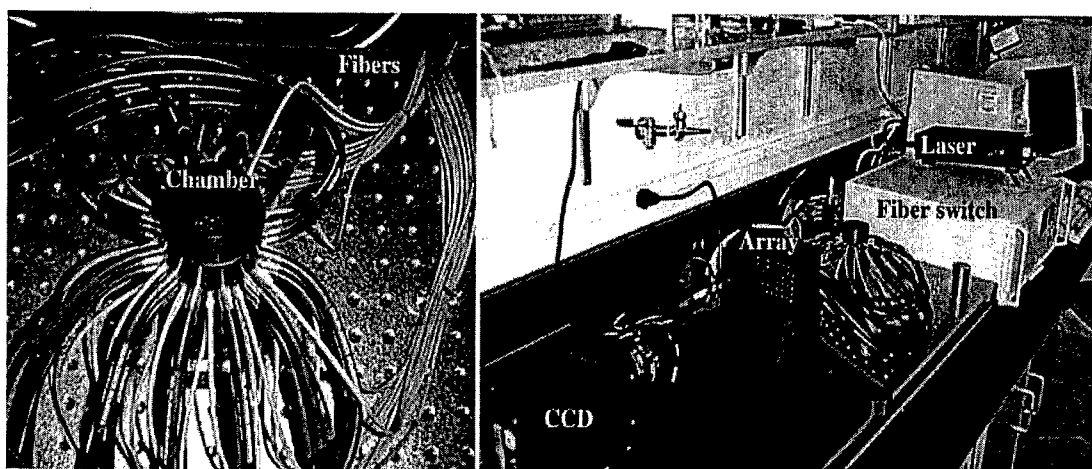


Fig. 4: System components (see text for details)

The FMT system consists of the following components (Fig. 4 and Fig.5): The light source (a) is a 670nm laser diode (B&W TEK Newark DE) operating in continuous wave mode with maximum power 200mW. This wavelength was selected for imaging the new infrared fluorochrome Cy5.5 (Amersham Pharmacia biotech Piscataway NJ), which has an absorption peak at 675nm and an emission peak at 694nm. Laser diodes at different wavelengths could be used to excite different fluorochromes. The light from the laser diode is directed to a 50/50 fused silica coupler (b) (OZ Optics Ontario Canada) that

splits the signal to the reference branch (c) and to the optical switch (d). The optical switch (Dicon FiberOptics CA) can multiplex one input to any of the 32 outputs. In the current implementation light is switched sequentially to only 24 outputs and directed onto the optical bore (f) using 24 200/230 μm multimode optical fibers (e) (Fiber Instrument Sales Oriskany NY). Three-millimeter diameter optical fiber bundles (Dolan-Jenner Industries MA) are used for light detection (g). The detection fibers are arranged in a 6x6 array onto a flat plate (h) made of DelrinTM. The fiber array is imaged with a Vers Array 512B back-illuminated CCD camera (Roper Scientific NJ) with ~80% quantum efficiency in the 700nm spectral range. The imaging lens is a 60mm F-mount Micro-Nikkor f/2.8D lens (Nikon JP). For fluorescence detection a three-cavity band-pass interference filter is used with center frequency at 705 nm and a full-width at half-maximum response of $\pm 5\text{nm}$ (Andover Corporation NH).

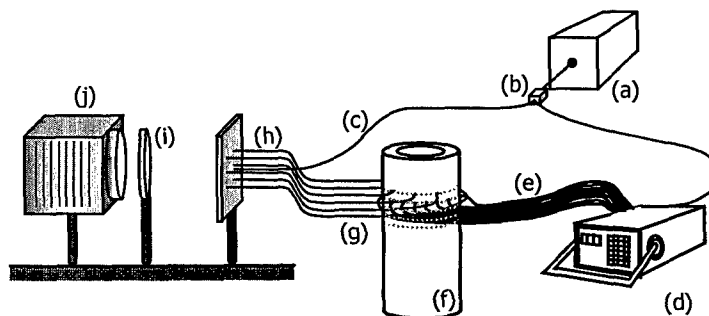


Fig. 5: System schematic (see text for details)

The optical bore (f) is the central piece of the device. It is made out of Delrin and has an inner diameter of 2.5cm and an outer diameter of 5cm. The optical fibers are inserted through the Delrin and come face to face with the inner wall. Three rings of 12 detector fibers are interlaced with 2 rings of 12 source fibers. The distance between rings is 0.5cm. The selected bore diameter can comfortably accommodate most mouse strains. The tube is water-sealed and is filled with a diffuse matching fluid to minimize photon wave mismatches within the cylinder. The matching fluid consists of water, an absorbing dye and Intralipid or TiO₂ particles at concentrations optimized to simulate tissue absorption and scattering. Phantoms and animals are inserted in the optical chamber. The selected diameter of 2.5 cm can accommodate all mouse models proposed.

Analytical instrument evaluation is included in the appendix (report #1).

Novel reconstruction algorithm

In addition to developing a system we also developed an appropriate self-calibrated algorithm for FMT imaging based on the general mainframe of perturbation algorithms previously developed for DOT^{11,12}. The specific algorithm developed⁴ capitalizes on the instrument ability to obtain intrinsic and fluorescence measurements and to construct differential measurements not using pre-/post- probe administration measurements but using absorption/fluorescence differential measurements. Specifically,

the intrinsic photon field divides the fluorescence measurement to normalize it and to cancel out instrument gain terms as well. In a manuscript recently published⁴ (see also appendix) we show the construction of the normalized field and of appropriate Greens functions and demonstrate that one could use only post-administration measurements to perform differential imaging. An advantage of this approach is that no instrument calibration is required. Furthermore, the algorithm developed is suited for imaging heterogeneous media because it has been shown that perturbative diffuse optical tomography methods perform very well when differential measurements are obtained¹³. Although the method is based on a linear analytical solution, the basic principle of using the intrinsic field to normalize fluorescence measurements can be used with higher order analytical or numerical solutions of the diffusion equation.

Analytical algorithm description and evaluation is included in the appendix (report #2).

Phantom measurements: calibration, quantitation, validation, sensitivity

Absorption Imaging. Phantom experiments were initially performed to verify the three-dimensional position and accuracy of measurements in both absorption and fluorescence mode. The experimental set-up is illustrated in Fig 6. Briefly, a phantom containing 3 capillary tubes (1 mm internal diameter), was constructed using a triangular geometry and inserted into the optical chamber containing a turbid medium (Intralipid). The capillaries were separated 8 and 11 mm from each other, and were coated with a black dye to maximize absorption. Fig. 6 depicts the reconstructed image at a plane perpendicular to the longitudinal axis of the imaging chamber, at about the middle of the three-dimensional volume. The reconstruction mesh used was $0.8 \times 0.8 \times 2 \text{ mm}^3$. The reconstruction used 24×36 measurements. Our data show that very good positional accuracy can be obtained using the standard perturbation based on the Rytov approximation. For this measurement the Greens functions are derived using a finite-difference solution of the diffusion equation assuming a homogeneous cylindrical medium with the Intralipid optical properties at 675 nm and bounded by a high absorption cylindrical boundary ($\mu_a=5\text{cm}^{-1}$).

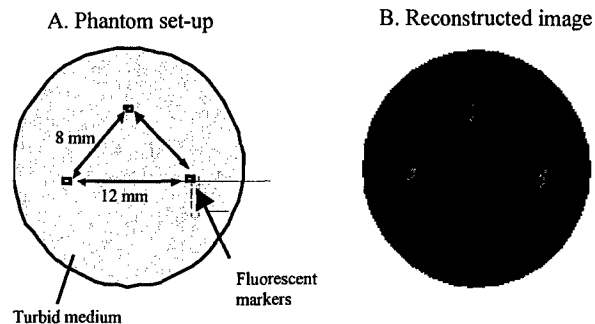


Fig. 6: Experimental set-up and actual reconstruction (right). Note the excellent spatial location of the capillary tubes

Sensitivity. Subsequent phantom experiments were performed to investigate the sensitivity of detection using non-quenched near infrared Cy5.5 dye. We inserted a 3 mm diameter, 2 cm long tube containing 200nM Cy5.5 in the optical bore (Fig. 7). The background intralipid solution had optical properties: $\mu_a=0.025 \text{ cm}^{-1}$ and $\mu_s'=5 \text{ cm}^{-1}$. The total fluorescent photon counts detected from two

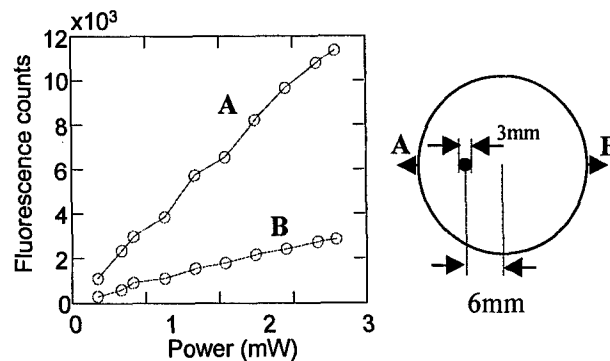


Fig. 7: Sensitivity of read-out of fluorochrome phantom in Intralipid.

opposite sides after noise subtraction are plotted as a function of light power. The light source was adjacent to position A and the integration time was 20 seconds. The data show that there is significant fluorescent signal detected at all positions. Increasing the laser power can significantly reduce acquisition times. Based on those measurements and appropriate solutions of the diffusion equation we can predict the equivalent photon counts expected in different geometries and tissues. For example within a slightly compressed breast of 5 cm width and optical properties $\mu_a=0.05\text{cm}^{-1}$ and $\mu_s'=10\text{cm}^{-1}$ the expected photon counts from a similar 3 mm volume and expected dye concentrations the maximum counts expected would be more than 2,500 above noise level using a 100 mW laser power. Other measurements in the laboratory with fluorometers using higher light powers suggest that the signal detected should scale linearly with light power for much higher powers used.

Quantitating fluorochrome concentration by imaging.

To determine the accuracy in estimating fluorochrome concentrations we also imaged a similar phantom as described above but containing different concentrations. Again, the optical bore was filled with 0.5% Intralipid (Fresenius Kabi Clayton L.P., NC) and 6 μM IC-Green (Akorn Inc. IL) yielding a liquid with $\mu_s'=7 \text{ cm}^{-1}$ and $\mu_a=0.05 \text{ cm}^{-1}$ at 675nm. Two glass tubes (3.5 mm inner diameter) were inserted with centers 12 mm apart. The tube on the left contained 500 nM Cy5.5 and the tube contained 750 nM Cy5.5. The reconstructed plane was interpolated to a 60 x 60 grid ($h'=0.04 \times 0.04 \text{ cm}^2$). Two objects were reconstructed and the accuracy of quantitating the true Cy5.5 concentration was $\pm 10\%$.

The result is shown in Fig. 8 and analytically in the appendix (report #2). The reconstruction accuracy can be further improved with larger data sets

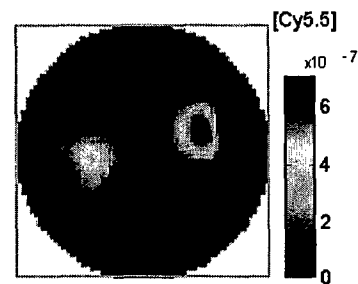


Fig. 8: Reconstructions of 2 phantoms containing different concentrations of Cy 5.5

Imaging of fluorescence activation.

In another experiment, quantitative, spatially localized information on fluorescence activation was obtained as a function of time. As shown in Fig. 9, a 3 mm tube was immersed into Intralipid, similarly as above. The tube contained 1.5 μM of a trypsin sensitive enzyme probe, which was activated by trypsin (100 μM) at time 0. Each single frame was acquired for 1 minute (12 sources at 5 sec acquisition each). The series of temporal snapshots on the right of Fig. 9 illustrate the reconstructed frames obtained at different time points. For example, at 20 minutes after trypsin addition, ~20% of the probe had been activated. At later time points, e.g. at 200 minutes after the enzyme was added, ~75% of the probe had been activated. These experimental data show that the developed FMT system can monitor with significant sensitivity and accuracy fluorescence activation transient phenomena as corroborated by parallel in vitro enzymologic measurements. It is expected, that the proposed improvements to the FMT system will 1) further improve the sensitivity by improving the light strength, 2) improve quantification accuracy but improving laser intensity stability and 3) improve acquisition speeds by appropriate automation and the proposed power increase.

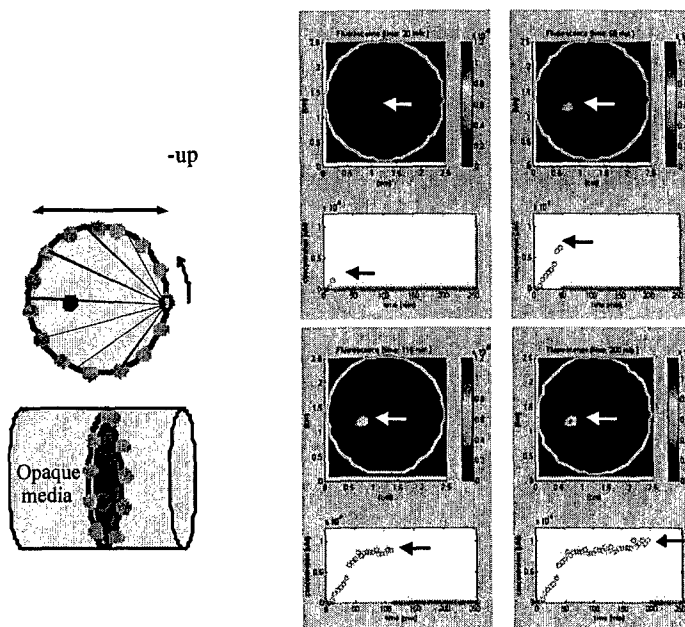


Fig. 9: Temporal imaging of enzyme activity in diffuse media (see text)

In-vivo imaging

We tested the novel imager with animal imaging as well. To perform validation we combined FMT measurements with anatomical and gadolinium enhanced MRI. For coregistration purposes the animals were placed in an appropriately constructed translucent insert (shown in Fig. 10) that was transferable between the optical and MR scanners to maintain positional certainty. We used this combined MRI and FMT scan to obtain maps of cathepsin B protease activity in human tumors implanted into nude mice (Fig. 11). The tumors were cathepsin B rich HT1080 fibrosarcoma, which had been implanted into the mammary fat pad of mice 7-10 days prior to the experiment. The animals received an IV injection of a cathepsin B sensitive imaging probe [Weissleder, 1999 #305] at 24 hours prior to the imaging experiments. The animals were anaesthetized with an intraperitoneal injection of 90 mg/kg ketamine and 9 mg/kg xylazine and were imaged by FMT (manual image acquisition was approximately 10 minutes).

Subsequently, the animals were removed from the imaging chamber. Fiducials with water were attached to predetermined positions on the periphery of the insert. The insert was subsequently placed in the MR coil and a set of axial T2-weighted images were obtained.

The role of the fiducials was to identify on the MR images the position of selected source and detector fibers for later co-registration of the images. Fig. 9 shows three corresponding slices obtained at tumor, heart and kidney levels. There was excellent congruence of optical and MR contrast from the tumor slice, known to have high cathepsin B activity as corroborated by immunohistochemistry and Western blotting. The cardiac/pulmonary slice (not shown here) demonstrated cathepsin B absence in those organs and the lowest slice (not shown here) shows renal presence of the enzyme as reported in the literature.

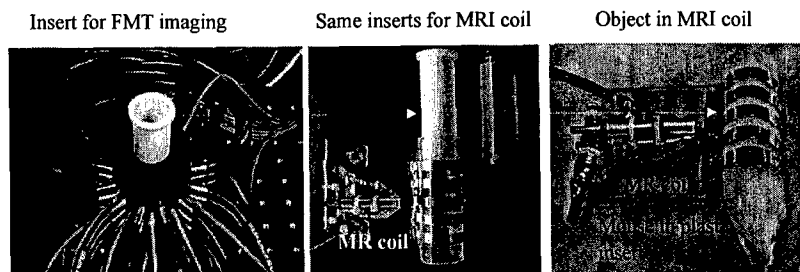


Fig. 10: Various mouse holders (inserts) for the FMT imaging system (left). The same inserts also fit snugly into home built-MR coils for combined MR/FMT imaging.

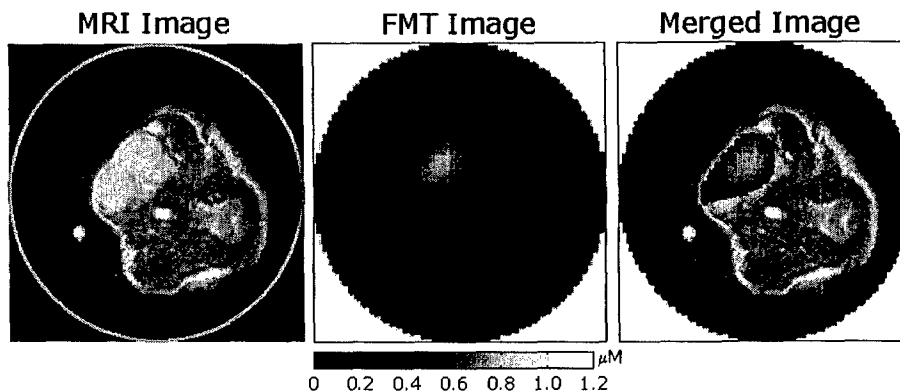


Fig. 11: Combined MR/FMT measurement at three body levels of a tumor bearing mouse. FMT measure the cathepsin B enzyme activity

To test whether the system and technique could investigate smaller tumors, implanted in deeper sites we selected a brain implantation site and imaged millimeter sized tumors at different depths. A report on that can be seen in the appendix (report #3).

Key Research Accomplishments

The key research accomplishments associated with the statement of work are as follows:

- 1) Construction of a fully operational FMT scanner prototype for animal imaging. The specifics of the instrument are included in the appendix (report #1).
- 2) Development of appropriate algorithms for in-vivo imaging that produce very accurate quantified images of the activation of smart fluorescent probes and molecular beacons.
- 3) Testing of the above instrument with phantom measurements to demonstrate femto-molar sensitivity to detect fluorescent probes [see appendix report 2] and the capacity to perform three-dimensional quantified imaging of fluorochromes in dense media [see appendix report 1].
- 4) In-vivo demonstration of non-invasively imaging cathepsin B activity in different sized tumors implanted at different depths, correlated with MRI, immuno-histochemistry and Western blotting.
- 5) Proof of feasibility that Fluorescence-mediated molecular tomography can be used as a novel workframe for examine molecular events in-vivo and in deep tissues.

Reportable outcomes

- 1) Paper in preparation regarding the instrument specifics.
- 2) Paper in preparation regarding in-vivo imaging.
- 3) Paper published (Ntziachristos et.al. Opt. Lett. **26**(12): 893-895 (2001)) on algorithmic development.
- 4) Presentation on FMT in High resolution in small animals conference 2001 (HiRes2001) held in Rockville Maryland, September 2001.
- 5) Invited presentation in Contrast Media Research 2001 (CMR 2001) held in Capri, Italy, October 2001.
- 6) R21/R33 grant submitted to NIH for continuation of instrument development.

Conclusions

We have developed an instrument and an imaging method and applied successfully to imaging cancer-associated expression of cathepsin B probes. We found that the technique offers superb sensitivity, quantification and localization accuracy. Clearly higher source detector systems could further improve the sensitivity, accuracy and resolution which in the current implantation is of the order of 2 mm. The technique could serve as the work platform for testing multiple other cancer associated enzymes or for gene expression profiling. Implementation of spectral capabilities could further enhance this approach since multiple targets could be investigated simultaneously by separating their contribution using fluorochromes emitting at different wavelengths. The former is of particular clinical relevance as "expression patterns" rather than single molecules may

form the basis for more sophisticated future imaging diagnostic techniques. Most importantly we have found that this technology could be transferable to human applications. NIR light has been shown to penetrate tissues several centimeters and detection is thus not necessarily limited to small volumes. Indeed, recent measurements and modeling [Ntziachristos, 2001 #30] show that near infrared fluorescent signals from tumor-like structures can propagate for more than 15 centimeters in breast or lung tissue and more than 5 cm in the adult brain. Again, these estimates may well be surpassed by newer detection technologies and/or more efficient beacons. While we chose to construct a cylindrical imaging chamber for mice, human imaging systems could well have different geometries for more efficient light collection. Planar imaging geometries, handheld scanners or even endoscopic sensors are all technologically feasible providing optimized approaches for imaging of specific organs or diseases. An important aspect to potential clinical tomographic imaging is the fact that FMT is inherently quantitative and can be acquired over time for monitoring purposes. Additional advantages include the fact that no radiation is required, that beacons and fluorochromes are usually stable and do not decay like isotopes and that the technology is relatively inexpensive compared to other tomographic imaging systems. Finally, FMT imaging should be useful for monitoring drug therapies at the molecular levels [Bremer, 2001 #21] over time and in tailoring treatments in individual patients. FMT imaging may also be a useful adjunct to x-ray computed tomography and magnetic resonance imaging. It is thus hoped that FMT imaging will find applications in unraveling complex biological pathways in murine models and in applying this knowledge to current problem areas in clinical diagnosis and drug testing.

References

- ¹R. Weissleder, "A clearer vision for in vivo imaging," *Nature Biotechnology* **19** (4), 316-317 (2001).
- ²V. Ntziachristos and B. Chance, "Probing physiology and molecular function using optical imaging: applications to breast cancer," *Breast Cancer Res* **3** (1), 41-46 (2001).
- ³C.T Tung, U Mahmood, S Bredow et al., "In vivo imaging of proteolytic enzyme activity using a novel molecular reporter," *Canc Res* **2000** (60), 4953-4958 (2000).
- ⁴V. Ntziachristos and R. Weissleder, "Experimental three-dimensional fluorescence reconstruction of diffuse media using a normalized Born approximation," *Optics Letters* **26** (12), 893-895 (2001).
- ⁵R Jain, "Delivery of molecular medicine to solid tumors," *Science* **271**, 1079-1080 (1996).
- ⁶J. E. Koblinski, M. Ahram, and B. F. Sloane, "Unraveling the role of proteases in cancer," *Clin Chim Acta* **291** (2), 113-35. (2000).
- ⁷L. J. McCawley and L. M. Matrisian, "Matrix metalloproteinases: multifunctional contributors to tumor progression," *Mol Med Today* **6** (4), 149-56. (2000).
- ⁸R. Weissleder, C.H. Tung, U. Mahmood et al., "In vivo imaging of tumors with protease-activated near-infrared fluorescent probes," *Nature Biotech* **17** (4), 375-8 (1999).
- ⁹C.H. Tung, S. Bredow, U. Mahmood et al., "Preparation of a cathepsin D sensitive near infrared fluorescence probe for imaging," *Bioconjug Chem* **10** (5), 892-896 (1999).
- ¹⁰C Bremer, C Tung, and R Weissleder, "Imaging of metalloproteinase2 inhibition in vivo," *Nature Med* **7** (6), 743-748 (2001).
- ¹¹M. A. Oleary, D. A. Boas, B. Chance et al., "Experimental Images of Heterogeneous Turbid Media By Frequency-Domain Diffusing-Photon Tomography," *Optics Letters* **20** (5), 426-428 (1995).
- ¹²M. A. Oleary, D. A. Boas, X. D. Li et al., "Fluorescence lifetime imaging in turbid media," *Optics Letters* **21** (2), 158-160 (1996).
- ¹³V. Ntziachristos, A. H. Hielscher, A. G. Yodh et al., "Diffuse optical tomography of highly heterogeneous media," *Ieee Transactions on Medical Imaging* **20** (6), 470-478 (2001).

APPENDIX

REPORT #1

CCD-based scanner for three-dimensional fluorescence-mediated diffuse optical tomography of small animals.

Vasilis Ntziachristos and Ralph Weissleder

Center for Molecular Imaging Research

**Massachusetts General Hospital & Harvard Medical School.
Charlestown MA 02129**

ABSTRACT

We present a novel tomographer for three-dimensional reconstructions of extrinsic fluorochromes distributed in small animals. The tomographer has been developed for studying novel classes of fluorescent agents useful in diagnostics and drug development. Photon detection is based on CCD technology and allows the implementation of a large parallel array of optical channels with high sensitivity. Using this instrument we studied the response and detection limits of near-infrared fluorochromes in diffuse media as a function of light intensity and for a wide range of biologically relevant concentrations. We further examined the resolution of the scanner and the reconstruction linearity achieved in the fluorescence mode. We demonstrate that the instrument attains better than 3mm resolution, is linear within more than two orders of magnitude of fluorochrome concentration and can detect fluorescent objects at sub-nanomolar fluorochrome concentrations.

INTRODUCTION

Diffuse Optical Tomography (DOT) is a medical imaging technique that collects light propagated through diffuse media, such as tissue, at multiple projections and reconstructs the internal distribution of optical properties ¹. Interestingly, the technique propagated directly from the laboratory bench to human applications, such as imaging of breast cancer ^{2 3}, brain function ⁴ and muscle ⁵ because of the non-invasiveness and safety of light radiation used. It would be of great interest however to develop instruments for tomographic animal investigations, particularly for in-vivo studies of novel contrast agents and fluorescent probes which are not yet approved for human use.

In this work we describe a tomographic scanner operating in fluorescence mode, developed specifically for imaging of small rodents. The scanner offers highly sensitive detection of fluorochromes and high capacity for parallel detection of a large number of optical fibers, in order to facilitate true three-dimensional reconstructions. We have recently reported on the capacity of the

scanner to perform quantitative three-dimensional reconstructions of fluorochromes using a newly developed fluorescence reconstruction algorithm⁶. Here we focus on studying key important experimental parameters on system performance and fluorochrome reconstructions, i.e. the detection sensitivity and the linearity of fluorescent signals as a function of fluorochrome concentration and incident light intensity. Additionally, we examine the linearity achieved in the reconstructed fluorescence images as a function of fluorochrome concentration. To the best of our knowledge this is the first systematic experimental evaluation of tomographic performance of fluorochromes embedded in diffuse media. To complete the study we also report on the signal to noise and the resolution achieved.

The remainder of this paper is divided in three sections. The first section describes the instrument developed and the reconstruction tools employed. The second section presents experimental measurements from fluorochromes embedded into diffuse media. Finally, the third section discusses the results and outlines the potential applications of this technology.

METHODS

Fluorescence animal tomographer

The system developed is shown in figure 1. The light source (a) is a 670nm laser diode (B&W TEK Newark DE) operating in continuous wave mode with maximum power 200mW. This wavelength was selected for imaging the new infrared fluorochrome Cy5.5 (Amersham Pharmacia biotech Piscataway NJ), which has an absorption peak at 675nm and an emission peak at 694nm. Laser diodes at different wavelengths could be used to excite different fluorochromes. The light from the laser diode is directed to a 50/50 fused silica coupler (b) (OZ Optics Ontario Canada) that splits the signal to the reference branch (c) and to the optical switch (d). The optical switch (Dicon FiberOptics CA) can multiplex one input to any of the 32 outputs. In the current implementation light is switched sequentially to only 24 outputs and directed onto the optical bore (f) using 24 200/230 μ m multimode optical fibers (e) (Fiber Instrument Sales Oriskany NY). Three-millimeter diameter optical fiber bundles (Dolan-Jenner Industries MA) are used for light detection (g). The detection fibers are arranged in a 6x6 array onto a flat plate (h) made of DelrinTM. The fiber array is imaged with a Vers Array 512B back-illuminated CCD camera (Roper Scientific NJ) with ~80% quantum efficiency in the 700nm spectral range. The imaging lens is a 60mm F-mount Micro-Nikkor f/2.8D lens (Nikon JP). For fluorescence detection a three-cavity band-pass interference filter is used with center frequency at 705 nm and a full-width at half-maximum response of ± 5 nm (Andover Corporation NH).

The optical bore (f) is the central piece of the device. It is made out of Delrin and has an inner diameter of 2.5cm and an outer diameter of 5cm. The bore is shown in more detail in figure 2. The optical fibers are inserted through the Delrin and come face to face with the inner wall. Three rings of 12 detector fibers are interlaced with 2 rings of 12 source fibers. The distance between rings is 0.5cm. The selected bore diameter can comfortably accommodate most mouse strains. The tube is water-sealed and is filled with a diffuse matching fluid to minimize photon wave mismatches within the cylinder. The matching fluid consists of water, an absorbing dye and Intralipid or TiO₂ particles at concentrations optimized to simulate tissue absorption and scattering.

Fluorescence Diffuse Optical Tomography

In this work we employed a normalized reconstruction algorithm reported earlier⁶ that operates on relative photon signals, thus facilitating minimum instrument calibration (in contrast to operating on absolute photon measurements). The algorithm, briefly described here for presentation completeness, uses measurements that can be obtained after dye administration and resolves absolute

fluorochrome concentrations; therefore it is ideally suited for in-vivo measurements. For every source-detector pair, the normalized fluorescence measurement U^{nB} can be constructed as:

$$U^{nB}(\vec{r}_s, \vec{r}_d) = \frac{1}{\Theta_f} \cdot \frac{U_f(\vec{r}_s, \vec{r}_d)}{U_{inc}(\vec{r}_s, \vec{r}_d)} \cdot \frac{QE^{\lambda_1}}{QE^{\lambda_2}} \quad (1)$$

where $U_f(\vec{r}_s, \vec{r}_d)$ is the fluorescence field detected at position \vec{r}_d due to a source at position \vec{r}_s and $U_{inc}(\vec{r}_s, \vec{r}_d)$ is the incident field, i.e. the photon field at the excitation wavelength for the same source detector pair. QE^{λ_1} , QE^{λ_2} are the detector quantum efficiencies at wavelength λ_1, λ_2 respectively and Θ_f is the attenuation of the filter that is used to collect the fluorescent field. The terms Θ_f and $QE^{\lambda_2}/QE^{\lambda_1}$ can be determined experimentally and are virtually independent of position and time. Therefore the term $U^{nB}(\vec{r}_s, \vec{r}_d)$ is independent of individual source-detector pair gain factors. It can be shown (see ref^{#6} and references therein) that $U^{nB}(\vec{r}_s, \vec{r}_d)$ can be written as a function of the medium's fluorochrome distribution, i.e.:

$$U^{nB}(\vec{r}_s, \vec{r}_d) = \frac{1}{U_0(\vec{r}_s, \vec{r}_d, k^{\lambda_1})} \cdot \int d^3r \cdot (U_0(\vec{r}_s - \vec{r}, k^{\lambda_1}) \frac{n(\vec{r})}{1 - i\omega\tau(\vec{r})} \frac{\nu}{D^{\lambda_2}} G(\vec{r}_d - \vec{r}, k^{\lambda_2})), \quad (2)$$

where D^{λ_2} is the diffusion coefficient at λ_2 , ν is the speed of light into the medium and $n(\vec{r})$ is the position dependent product of the fluorochrome absorption coefficient $\mu_a(\vec{r})$ and fluorescence quantum yield γ . The parameters k^{λ_1} , k^{λ_2} are the wave propagation vectors⁷ at wavelengths λ_1, λ_2 respectively and $\tau(\vec{r})$ is the fluorescence lifetime of the fluorochrome at position \vec{r} . Eq.2 is written for the general case where the source term is light of modulated intensity ω . In the constant wave case $\omega=0$ and the fluorescence lifetime $\tau(\vec{r})$ does not contribute to the detected photon field. The function $U_0(\vec{r}_s, \vec{r}, k^{\lambda_1})$ describes the established photon field into the diffuse medium at position \vec{r} due to a source at position \vec{r}_s and $G(\vec{r}_d - \vec{r}, k^{\lambda_2})$ is the Green's function solution to the diffusion equation and describes the propagation of the emission photon wave from the fluorochrome at position \vec{r} to the detector at \vec{r}_d . Eq.2 treats fluorochromes as two-level quantum systems and ignores fluorescence saturation effects and high-order scattering interactions. These approximations are generally met at low fluorochrome concentrations. We also demonstrate experimentally in the results section that saturation effects are not observed over more than two orders of magnitude of biologically relevant fluorochrome concentrations.

For reconstruction purposes Eq. 3 is discretized into a number of volume elements (voxels), which yields a set of coupled linear equations. The terms U_0 and G are calculated numerically or analytically for the appropriate boundary conditions and background optical properties at λ_1 and λ_2 respectively. In this work the functions U_0 and G were calculated for the cylindrical boundary using a three-dimensional finite-difference solution of the homogenous diffusion equation for the background medium with discretization step $h=0.5\text{mm}$. The zero-boundary condition⁸ was assumed at $1/\mu'_s$ outside the actual boundary. The resulting system of equations is then inverted for the unknown quantity $n(\vec{r})$ using the Algebraic Reconstruction Technique with relaxation parameter $\rho=0.1$. Finally fluorochrome concentration $[F(\vec{r})]$ is calculated as $[F(\vec{r})] = n(\vec{r})/\gamma \cdot \epsilon$, where ϵ is the fluorochrome's extinction coefficient.

RESULTS

This section describes experimental measurements that outline the instrument performance and the reconstruction capacity pertaining to quantification accuracy, linearity, sensitivity and resolution.

Signal to noise ratio

To characterize the signal to noise ratio (SNR) of the instrument we performed measurements of intrinsic light (without the fluorescence filter) employing one source and all 36 detectors. Signal intensity was adjusted so that maximum signal was obtained without saturating any of the CCD pixels. Then 200 measurements on a diffuse medium ($\mu_s=0.02\text{cm}^{-1}$ $\mu_t=10\text{cm}^{-1}$) were sequentially acquired over a period of 5 minutes. This time is representative of typical acquisition times at full three-dimensional tomographic mode. The integration time per measurement was 0.1 sec. The signal to noise ratio in decibels (dB) was calculated as $SNR = 20 \cdot \log_{10}(\bar{S} / \sigma)$ where \bar{S} was the mean intensity of the detected signal S after background subtraction and σ was its standard deviation. The results for all 36 detectors employed are shown in figure 3. The average SNR obtained was ~50dB.

The main source of noise, besides the expected Poisson-distributed photonic noise and CCD read noise, was the intensity fluctuation of the laser source. The signal to noise ratio can be improved using the reference fiber measurements to monitor laser fluctuations as a function of time and accordingly correct the measurements. Figure 3 depicts the signal to noise ratio achieved for all 36 detectors after data correction. Correction consists of dividing all detector measurements at each time point with the reference measurement obtained at the same time point and multiplying the result with the maximum reference value observed throughout the 200 measurements. The SNR improvement observed after correction is approximately 7dB, since long-term drift and other fluctuations can be effectively accounted for.

Resolution

The resolution of tomographic techniques in the diffuse regime is a function of the number of sources and detectors employed, their geometrical arrangement, the overall dimension and optical properties of the medium of investigation and the signal to noise ratio. Furthermore, the resolution achieved is not uniform but it decreases as a function of depth. Here, we have investigated the capacity of the scanner to resolve two fluorophores at the middle of the optical bore, which represents a worst resolution case. We inserted two Pasteur glass tubes at the middle of the optical bore as shown in figure 4a. The tubes had an outer diameter of ~1.5mm, an inner diameter of ~1.2mm inner and were filled with 800nM of Cy5.5. The optical bore was filled with Intralipid and ink and attained a background absorption coefficient $\mu_a=0.05\text{cm}^{-1}$ and reduced scattering coefficient $\mu_s'=8\text{cm}^{-1}$. The two tubes were placed at different distances to each other and imaging was performed to identify the resolution limit.

Figure 4b and c depict the reconstructions achieved when the tubes were placed with a clear gap of 3mm and 2.8 mm apart. In both cases the two objects are resolved but at the shorter distance symmetry is lost. When the objects were placed even closer to each other, the asymmetry increased until only a single object was resolved. The appearance of asymmetry is mainly due to noise, which affects the ill-posed inversion problem. It should be noted that the instrument constructed is not built to favor resolution since only 12 measurements per ring are obtained. Increasing the number of sources and detectors along the periphery can further improve resolution, due to the higher spatial sampling but also due to the inherent improvement in signal to noise ratio⁹. Nevertheless, under the

current implementation, the resolution of the imager build is better than 3mm, especially since the phantom examined is a worse resolution case.

Fluorescence as a function of concentration and light intensity.

A key parameter of DOT in fluorescence mode is the emission signal response as a function of light intensity and fluorochrome concentration. Deviation from a linear behavior indicates photo-bleaching or quenching phenomena that could result in quantification errors and data misinterpretation. In order to investigate fluorescence responses, we inserted a fused quartz tube (Wilmad Glass NJ) into the optical bore as shown in figure 5. The tube was 4mm in inner diameter and 8mm in height and was sequentially filled with different concentrations of Cy5.5. Then fluorescence readings were obtained for different source detector pairs and varying incident light intensity. The acquisition time (integration time) was 5 sec. The concentration range examined was [1nM – 800nM] and represents a wide span of biologically expected fluorochrome accumulations. Figure 6 depicts the fluorescence counts obtained as a function of laser power for the different fluorochrome concentrations examined. For each light power selected, the fluorescence count plotted is the actual fluorescence measurement minus the background signal recorded by the same detector at 0nM fluorochrome concentration. Figures 6a and 6b are the linear and semi-logarithmic plots of the fluorescence counts obtained from the detector marked in figure 5 with the letter 'Y'. Similarly, figures 6c and 6d are the linear and semi-logarithmic plots of the fluorescence counts obtained for the detector marked in figure 4 with the letter 'Z'.

Figure 6 demonstrates a linear response for the entire range of light powers and concentrations. This finding indicates that no self-quenching effects or photo-bleaching occur with the investigated indocyanine dye. Furthermore concentrations of 1nM are clearly detectable, even when using low light power. This is particularly evident on the semi-logarithmic plots. By appropriately selecting the light power sub-nM concentrations could be also detected for smaller volume fractions.

Fluorescence reconstructions.

The feasibility to three-dimensionally reconstruct and quantify fluorochromes embedded in diffuse media with the herein reported instrument has been demonstrated recently ⁶. In this section we investigate another aspect of the reconstruction performance, i.e. the linearity of the reconstructed fluorochrome concentration as a function of the real fluorochrome concentration. Although a linear relation between fluorescence signals and fluorochrome concentrations was shown in Figure 6, tomographic techniques based on perturbation methods have been reported to give non-linear responses ¹⁰ and underestimate the perturbation magnitude as this magnitude increases. This is because perturbation methods operate optimally on the approximation that the perturbation signal detected is very small compared to the intrinsic signal (i.e. the signal at the excitation wavelength).

To examine the tomographic performance we reconstructed images of the embedded fluorochrome seen in Figure 5 for the range of concentrations examined in Figure 6 i.e. [1nM – 800nM]. The laser power used in all reconstructions was 30mW at the fiber tip and the acquisition time (integration time) was 10 seconds per source resulting in a 4-minute acquisition time for a full three-dimensional reconstruction. The reconstruction segmented the field of view in three slices with 700 voxels per slice. The voxel size was $\sim 1 \times 1 \times 8.3 \text{ mm}^3$. The inversion technique used was an iterative algebraic reconstruction technique (ART), which was run until one hundred more iterative steps yielded a change that was less than 1%. The typical number of iterative steps was ~ 2000 .

A typical reconstructed image is seen in Figure 7a. The image shown is interpolated to a 4 x 4 finer grid than the original. Figure 7b plots the reconstructed chromophore concentration as a function of the expected concentration. The reconstructed value demonstrates a remarkably linear response for the whole range of examined concentrations. It is possible that perturbation methods applied in the fluorescence regime attain a larger concentration range of linearity compared to absorption/scattering reconstructions. This could be due to the low fluorochrome quantum yield

that makes fluorescent perturbation signals much smaller than the corresponding absorption or scattering perturbation signals.

DISCUSSION

We have developed an imager for three-dimensional reconstructions of the distribution of fluorochromes in diffuse media and presented key performance characteristics. The detection fiber array coupling onto the CCD via a lens system allows great flexibility in employing a large number of parallel channels. A set of 144 fibers can be easily added with the same coupling characteristics as the 36 fibers investigated here. An arbitrary large number of fibers can be added by constructing a larger detection fiber array. Consequently however the field of view acquired by the lens system should increase which will induce additional coupling losses. Generally, a balance between the detector array size and the coupling efficiency should be achieved to attain an optimum design for any given application.

A particularly attractive feature of the fluorescent tomographer is that sub-nanomolar concentrations of fluorescent dyes contained into tumor-sized volumes can be detected. The present scanner was found sufficient to detect 1nM of Cy5.5 contained in $\sim 100 \mu\text{L}$. Lower concentrations or volumes could be detected by increasing light intensity and acquisition times. More sensitive cameras with lower noise floors (up to 2 orders of magnitude for liquid nitrogen cooled CCD cameras) could also be used to further improve sensitivity. In general, the sensitivity levels achieved approach those of nuclear imaging techniques and are several orders of magnitude lower than the sensitivity for detection of magnetic probes by Magnetic Resonance Imaging or x-ray absorbers by Computed Tomography.

We have further demonstrated that the instrument can produce quantified images and that it has a linear response for over two orders of magnitude of biologically relevant concentrations. Generally, the linearity across the board of parameters examined is an important finding since no correction schemes are required and high quantification accuracy can be achieved.

The technology presented here is geared towards examining animals implanted with certain diseases such as tumors, especially as pertaining to the bio-distribution of targeted and activatable fluorochrome reporter probes ¹¹. The specific geometry and dimensions are optimized for mouse imaging. Accommodation of different size animals can be achieved by using a different size optical bore. Although a large optical bore could in principle be used for smaller animals as well, optimizing the bore size for the animal size of interest facilitates minimum diffusion and optimal photon coupling.

Imaging of living tissues may impose complexities since different background absorption or scattering and spatial variations in the background optical properties may result in signals that are different from the ones obtained in our bench studies using simple homogeneous media. However, the reconstruction algorithm employed is specifically designed for tissue measurements. This is because the algorithm provides for a differential scheme where the intrinsic light normalizes the fluorescence measurement to cancel out or minimize the sensitivity to local and global gain factors and to heterogeneous photon propagation. An added advantage is that this normalization measurement can be obtained virtually simultaneously with the fluorescence measurement so that no recordings before fluorochrome administration are required. The performance of this imager with transgenic mouse models, and the cross-examination of the imaging results with other imaging techniques is currently under investigation.

FIGURE CAPTIONS

Figure 1. The animal tomographer constructed.

Figure 2. Optical bore. The sources and detectors are arranged in different rings to allow for three-dimensional reconstructions.

Figure 3. Experimental signal to noise ratio of the instrument. The right part of the histogram depicts the signal to noise ratio achieved for different source detector pairs when the reference measurement is used for data post-processing. The right part of the histogram plots the signal to noise achieved when no correction is applied.

Figure 4. a) Experimental set-up that investigated the instrument's resolution. The two objects shown are 1.5mm capillary tubes, 3 mm apart, containing 800nM of Cy5.5 dye. b) Reconstruction achieved with the fluorochromes inserted at 4% intralipid ($\mu_s' = 5\text{cm}^{-1}$). c) Reconstruction achieved using 8% intralipid ($\mu_s' = 5\text{cm}^{-1}$).

Figure 5. Experimental set-up that used to investigate the fluorescence responses and the reconstruction linearity of the technique.

Figure 6. Fluorescence responses from the experimental set-up plotted in figure 5. The top line depicts in linear and semi-logarithmic plots the responses detected by detector Y (c.f. figure 5). Bottom line depicts in linear and semi-logarithmic plots the responses detected by detector Y (c.f. figure 5).

Figure 7. a) Fluorescence reconstruction of the experimental arrangement in figure 5. The figure shown is the top slice of a three-slice reconstruction. b) Reconstructed fluorochrome concentrations as a function of expected fluorochrome concentrations.

REFERENCES

- ¹S. R. Arridge, "Optical tomography in medical imaging," *Inverse Problems* **15** (2), R41-R93 (1999).
- ²B. W. Pogue, S. P. Poplack, T. O. McBride et al., "Quantitative Hemoglobin Tomography with Diffuse Near-Infrared Spectroscopy: Pilot Results in the Breast," *Radiology* **218** (1), 261-266. (2001).
- ³V. Ntziachristos and B. Chance, "Probing physiology and molecular function using optical imaging: applications to breast cancer," *Breast Cancer Res* **3** (1), 41-46 (2001).
- ⁴D. A. Benaron, S. R. Hintz, A. Villringer et al., "Noninvasive functional imaging of human brain using light," *Journal of Cerebral Blood Flow and Metabolism* **20** (3), 469-477 (2000).
- ⁵E. M. C. Hillman, J. C. Hebden, M. Schweiger et al., "Time resolved optical tomography of the human forearm," *Physics in Medicine and Biology* **46** (4), 1117-1130 (2001).
- ⁶V. Ntziachristos and R. Weissleder, "Experimental three-dimensional fluorescence reconstruction of diffuse media using a normalized Born approximation," *Optics Letters* **26** (12), 893-895 (2001).
- ⁷M. A. O'Leary, D. A. Boas, X. D. Li et al., "Fluorescence lifetime imaging in turbid media," *Optics Letters* **21** (2), 158-160 (1996).
- ⁸A. Kienle and M. S. Patterson, "Improved solutions of the steady-state and the time-resolved diffusion equations for reflectance from a semi-infinite turbid medium," *Journal of the Optical Society of America a-Optics Image Science and Vision* **14** (1), 246-254 (1997).
- ⁹J. Culver, V. Ntziachristos, L. Zubkov et al., "Data set size and image quality in diffuse optical mammography: evaluation of a clinical prototype." in *Advances in Optical Imaging and Photon Migration*, OSA Technical Digest (Optical Society of America,), 392-394 (2000).

¹⁰AC Kak and M. Slaney, *Principles of Computerized tomographic imaging* (IEEE Press, New York, 1988).

¹¹R. Weissleder, "A clearer vision for in vivo imaging," *Nature Biotechnology* **19** (4), 316-317 (2001).

Figure 1

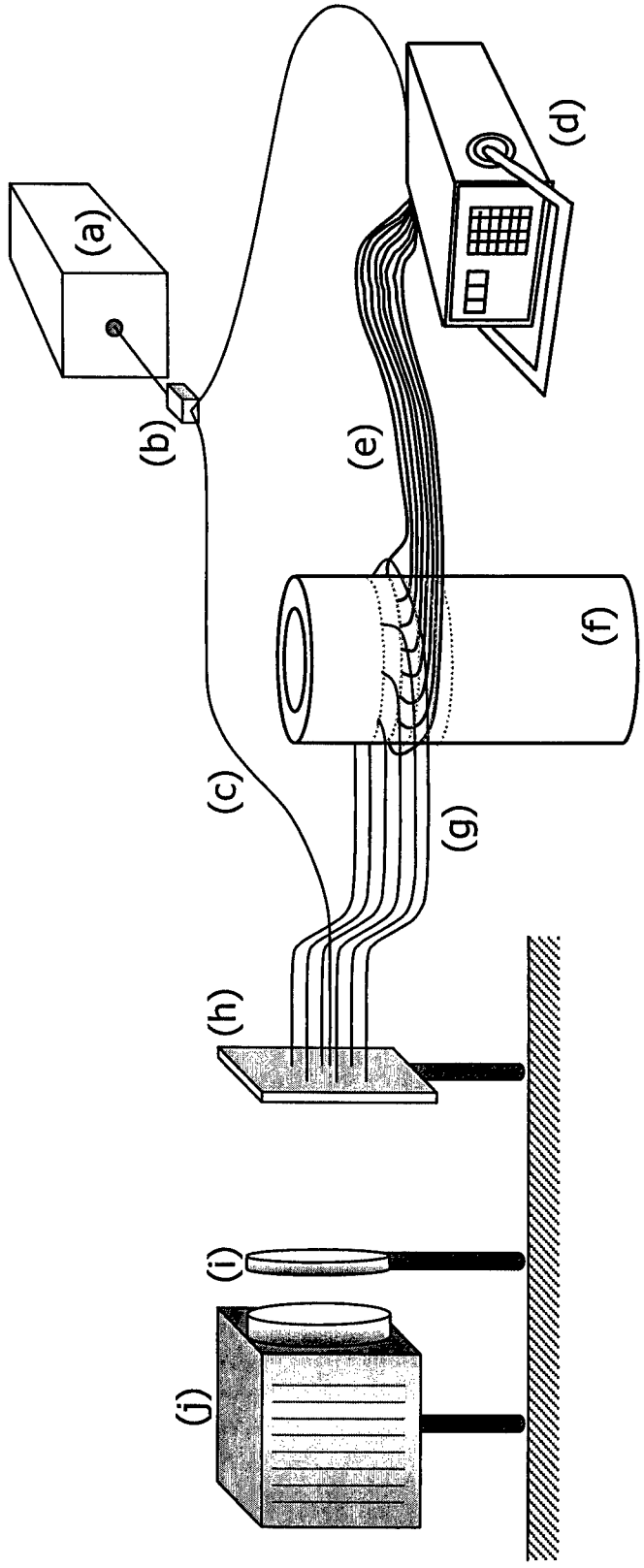


Figure 2

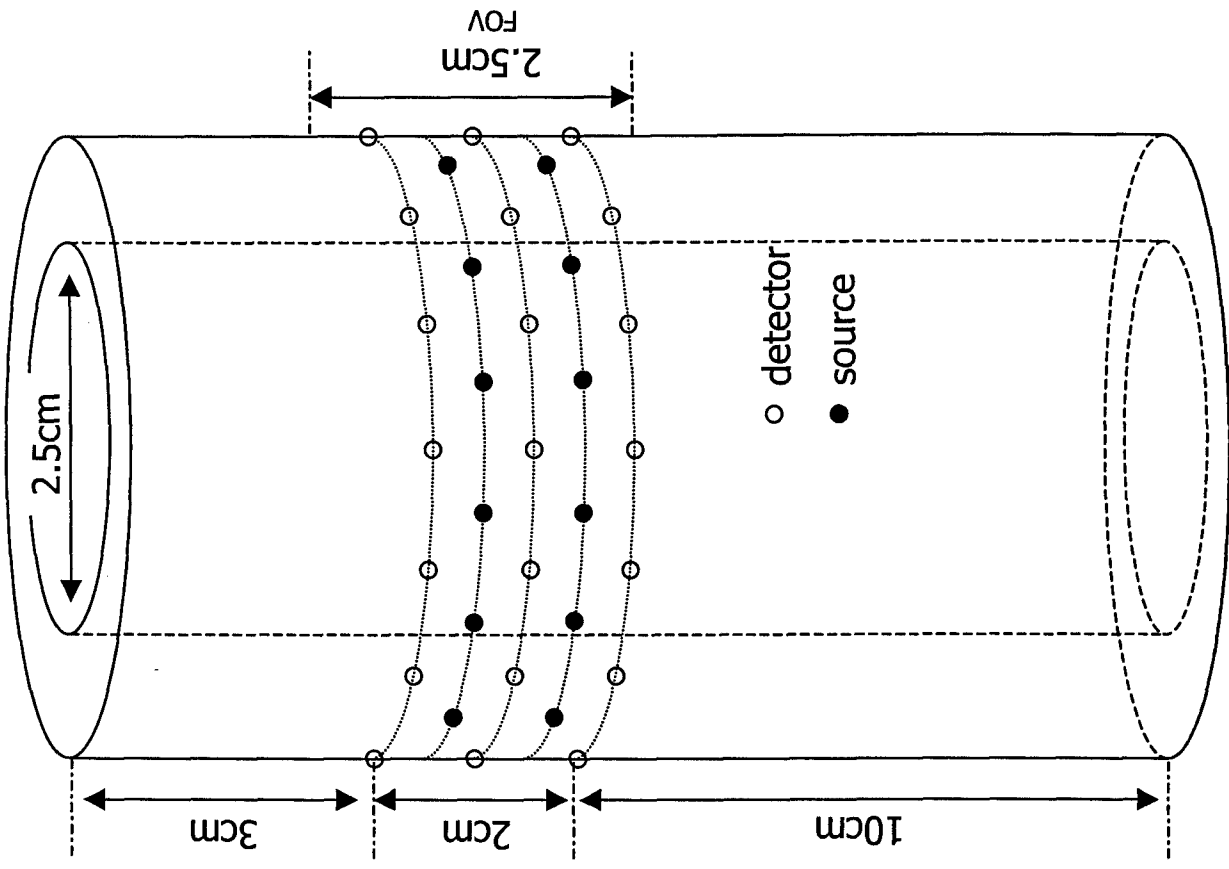


Figure 3

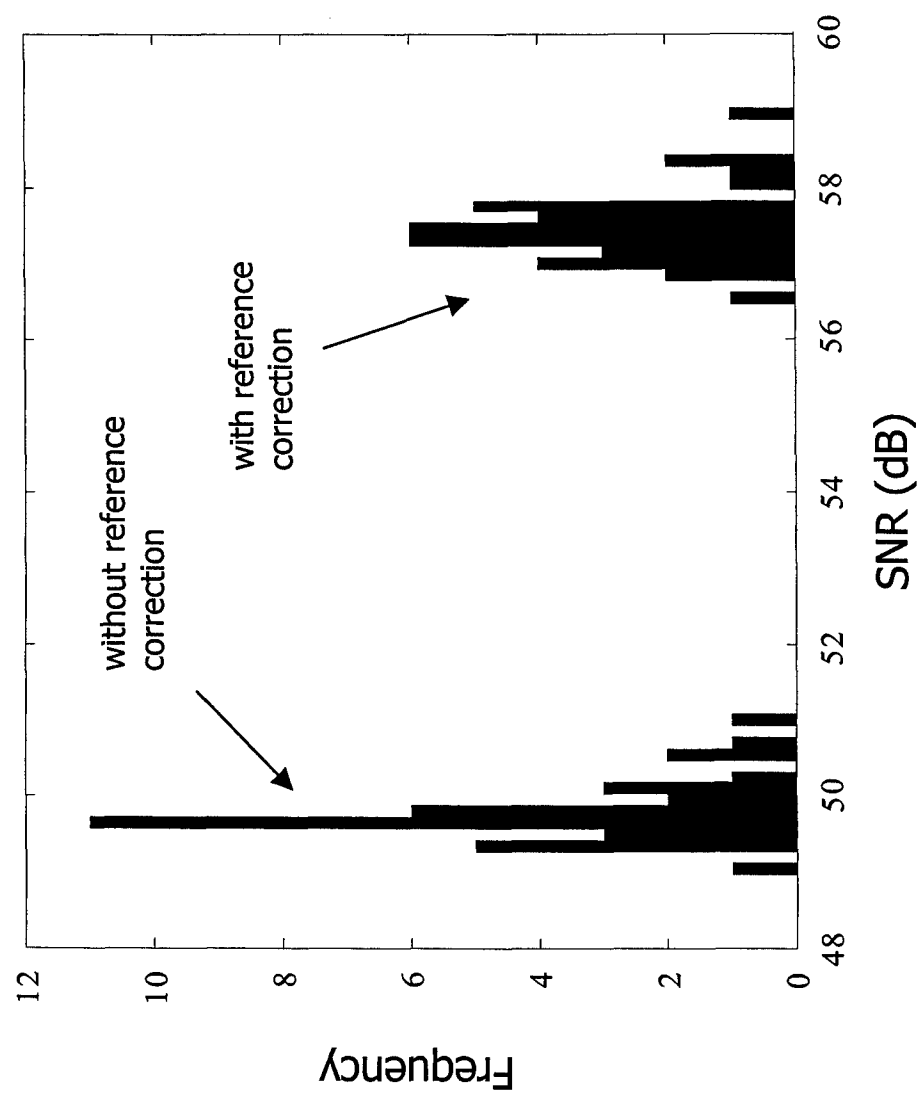
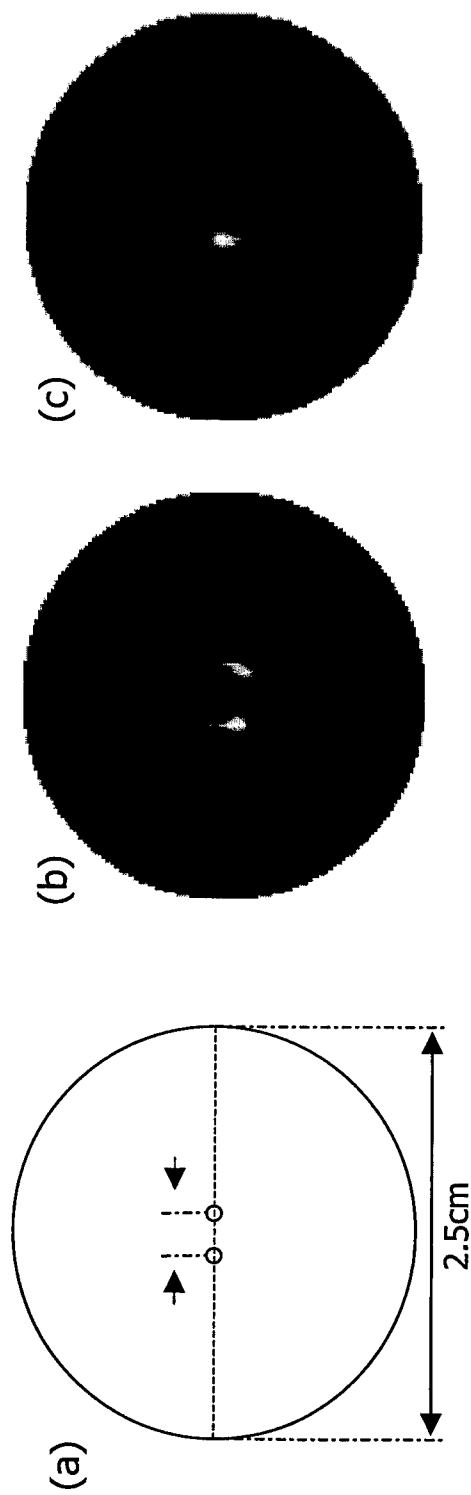


Figure 4



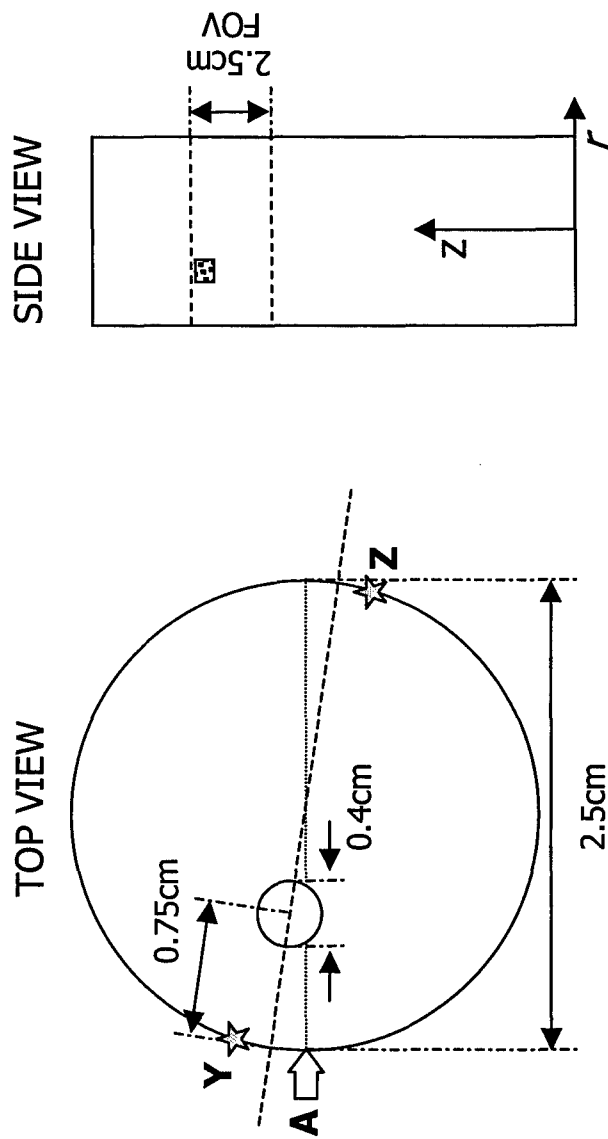


Figure 5

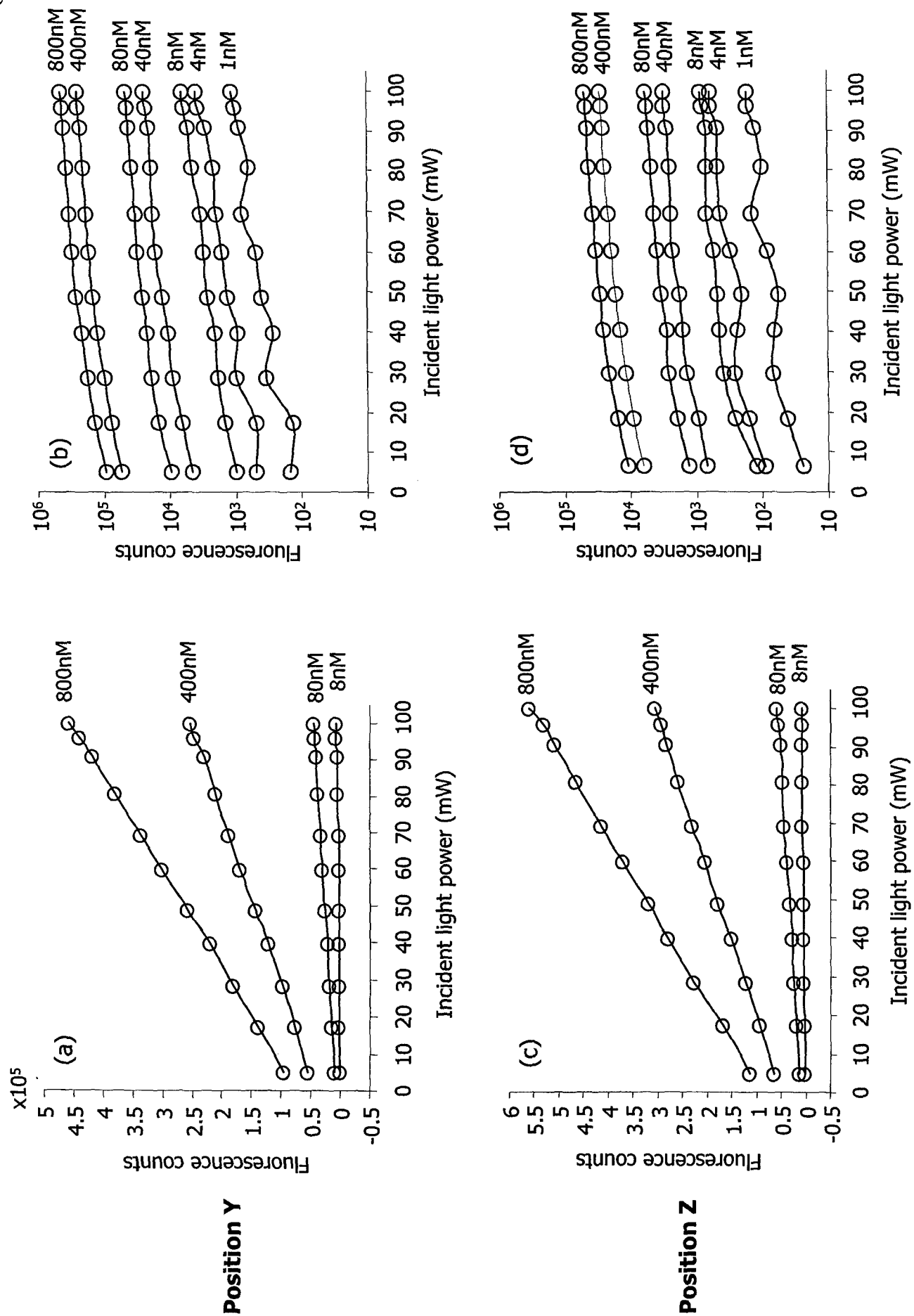
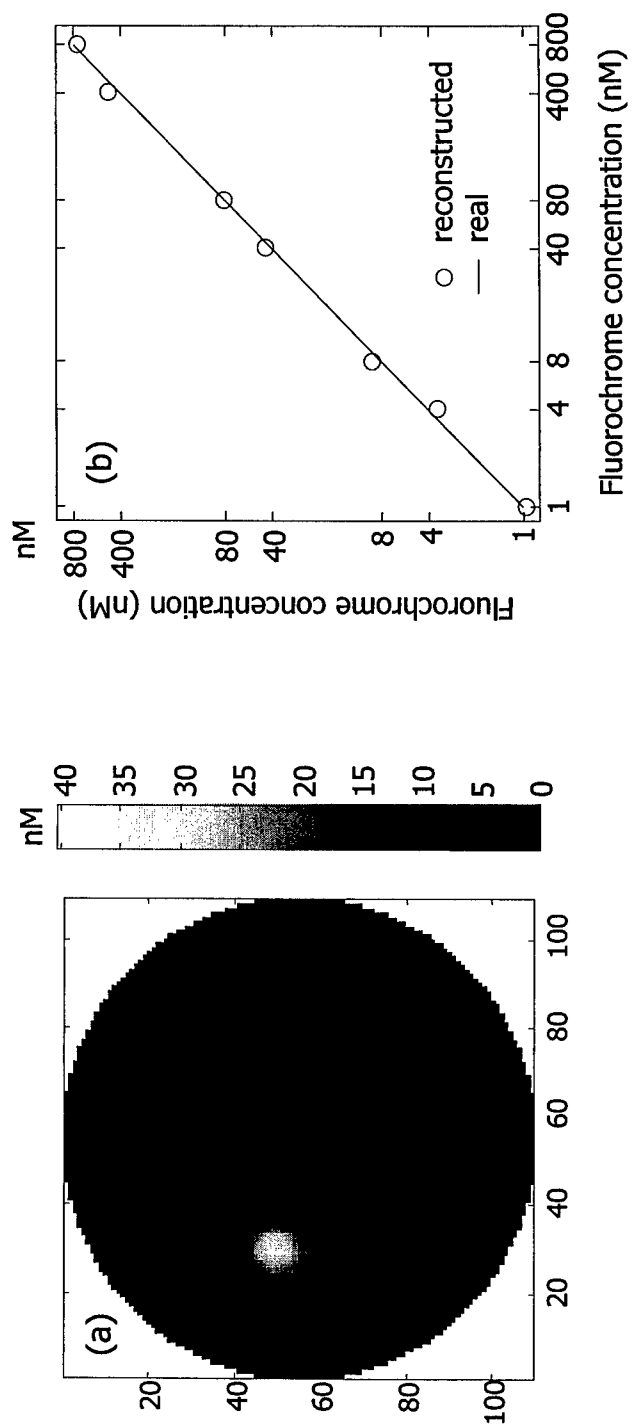


Figure 6

Figure 7



REPORT #2

Experimental three-dimensional fluorescence reconstruction of diffuse media using a normalized Born approximation.

Vasilis Ntziachristos and Ralph Weissleder

Center for Molecular Imaging Research

Massachusetts General Hospital & Harvard Medical School.
Charlestown MA 02129

Abstract

We present a normalized Born expansion that facilitates fluorescence reconstructions in turbid, tissue-like media. The algorithm can be particularly useful for tissue investigations of fluorochrome distribution in-vivo since it does not require absolute photon-field measurements or measurements before contrast agent administration. This unique advantage can be achieved only in fluorescence mode. We used this algorithm to three-dimensionally image and quantify an indocyanine fluorochrome phantom, using a novel fluorescence tomographic imager developed for animals.

Three dimensional tomography and quantification of fluorochrome bio-distribution in deep tissue will soon be necessary for imaging novel Indocyanine derivatives¹, targeted dyes² and smart molecular beacon-like agents³ that enable functional and molecular characterization of normal and diseased tissues. Tomographic approaches for fluorescence imaging in the NIR have been developed in the past^{4,5,6} and are straightforward expansions of algorithms originally developed for diffuse optical tomography (DOT) of absorption and scattering. In this Letter we present an algorithm that offers significant experimental advantages because it can work with measurements taken only from the target medium after fluorochrome administration; no pre-administration measurements or phantom measurements are required. This could be essential for in-vivo measurements and is a *unique* advantage of DOT in fluorescent mode. The algorithm is demonstrated using an analytical, linear solution of the diffusion equation but the principle of operation can apply to non-linear and numerical solutions. Experimentally, we found this algorithm very robust in imaging and quantifying the

three-dimensional distribution of two fluorochromes of different concentrations embedded into tissue-like media using a novel homemade animal imager.

The algorithm developed is based on a previously reported mainframe that uses a Born-type approximation to predict the forward field of photon propagation in diffuse media⁶. The photon wave detected in a non-bounded diffuse medium at position \vec{r} due to an intensity-modulated source at position \vec{r}_s is⁷ $U_0(\vec{r}_s, \vec{r}, \omega) = \Theta_s(\vec{r}_s) \exp(ik\vec{r}) / 4\pi D\vec{r}$, where $k = ((-\nu\mu_a + i\omega)/D)^{1/2}$ is the photon wave propagation vector, ν is the speed of light into the medium, ω is the angular modulation frequency, μ_a is the absorption coefficient, $D = \nu/3\mu'_s$ is the diffusion coefficient, μ'_s is the reduced scattering coefficient and $\Theta_s(\vec{r}_s)$ is a gain factor associated with light source strength, fiber coupling losses and other attenuation in the optical system. If $\Theta_d(\vec{r}_d)$ accounts for the detector gain and the detection fiber losses and QE^{λ_1} is the detector quantum efficiency at wavelength λ_1 , then the incident photon field detected at position \vec{r}_d is:

$$U_{inc}(\vec{r}_s, \vec{r}_d) = QE^{\lambda_1} \cdot \Theta_s(\vec{r}_s) \cdot \Theta_d(\vec{r}_d) \cdot U_0(\vec{r}_s - \vec{r}_d, k^{\lambda_1}), \quad (1)$$

where k^{λ_1} denotes the wave propagation vector for the optical properties of the medium of investigation at wavelength λ_1 .

When fluorescent objects exist in the medium, the field $U_f(\vec{r}_s, \vec{r}_d)$ detected at position \vec{r}_d at the emission wavelength can be written as^{6,8}:

$$U_f(\vec{r}_s, \vec{r}_d) = \int d^3r \cdot \Theta_s(\vec{r}_s) \cdot \Theta_f \cdot QE^{\lambda_2} \cdot \Theta_d(\vec{r}_d) \cdot U_0(\vec{r}_s - \vec{r}, k^{\lambda_1}) \cdot \frac{n(\vec{r})}{1 - i\omega\tau(\vec{r})} \cdot \frac{\nu}{D^{\lambda_2}} \cdot G(\vec{r}_d - \vec{r}, k^{\lambda_2}) \quad (2)$$

where $n(\vec{r})$ is the product of the fluorochrome absorption coefficient and fluorescence quantum yield, $\tau(\vec{r})$ is the fluorescence lifetime, k^{λ_2} is the wave propagation vector at wavelength λ_2 , Θ_f is the attenuation of the filter that is used to collect the fluorescent field and QE^{λ_2} is the detector quantum efficiency at the emission wavelength.

$G(\vec{r}_d - \vec{r}, k^{\lambda_2})$ is the Green's function solution to the diffusion equation and describes the propagation of the emission photon wave from the fluorochrome to the detector. Eq.2 treats fluorochromes as two-level quantum systems and ignores fluorescence saturation effects and high-order scattering interactions. These approximations hold for the weak fluorescent concentrations expected in many biological systems.

Finding solutions for Eq.2 requires determination of the factors $\Theta_s(\vec{r}_s)$, $\Theta_d(\vec{r}_d)$ for each source-detector pair \vec{r}_s, \vec{r}_d . To reach more manageable expressions for the fluorescent field we can divide Eq.2 by Eq.1 and rearrange to obtain the *normalized fluorescence Born field* U^{nB} , i.e:

$$\begin{aligned}
U^{nB}(\vec{r}_s, \vec{r}_d) &= \frac{1}{\Theta_f} \cdot \frac{U_f(\vec{r}_s, \vec{r}_d)}{U_{inc}(\vec{r}_s, \vec{r}_d)} \cdot \frac{QE^{\lambda_1}}{QE^{\lambda_2}} = \\
&= \frac{1}{U_0(\vec{r}_s, \vec{r}_d, k^{\lambda_1})} \cdot \int d^3r \cdot (U_0(\vec{r}_s - \vec{r}, k^{\lambda_1}) \frac{n(\vec{r})}{1 - i\omega\tau(\vec{r})} \frac{v}{D^{\lambda_2}} G(\vec{r}_d - \vec{r}, k^{\lambda_2}))
\end{aligned} \tag{3}$$

Eq.3 is similar to expressions obtained for the linear perturbation DOT problem using the Rytov approximation^{9,10} and offers experimental advantages because all the position dependent gain factors are cancelled out. The terms Θ_f and $QE^{\lambda_2}/QE^{\lambda_1}$ can be determined experimentally and are virtually independent of position and time. Usually, $QE^{\lambda_2}/QE^{\lambda_1} \approx 1$ due to the proximity of λ_1, λ_2 .

Eq.3 assumes a measurement of the incident field U_{inc} , i.e. a measurement through a homogeneous medium. This measurement is not practical when probing biological media. However, it has been shown¹¹ that U_{inc} can be substituted by a measurement U'_{inc} , obtained through the heterogeneous medium if U_0 at the right part of Eq. 3 is computed for the average optical properties of the medium at λ_1 (assuming a random, weak optical background heterogeneity). It is important to note that U'_{inc} can be obtained even if the fluorochrome is present during the measurement. The weak sensitivity of the algorithm to the selection of U_{inc} vs. U'_{inc} is demonstrated in the experimental section of this work and is a significant and unique advantage of the fluorescence-mode DOT compared to differential absorption/scattering DOT. This is because DOT of absorption/scattering requires a measurement before fluorochrome administration¹², which may not be always available, due to the long circulation times required by some fluorochromes for proper target accumulation.

For reconstruction purposes Eq. 3 is discretized into a number of volume elements (voxels), which yields a set of coupled linear equations. The terms U_0 and G can be calculated numerically or analytically for the appropriate boundary conditions and background optical properties at λ_1, λ_2 respectively. The resulting system of equations can then be inverted⁹ for the unknown quantities $n(\vec{r})$ and $\tau(\vec{r})$.

To demonstrate the algorithmic performance we used a novel animal optical tomographer with 24 source and 36 detector fibers arranged in five equidistant rings around a cylinder as shown in Figure 1. The cylinder was filled with 0.5% Intralipid (Fresenius Kabi Clayton L.P., NC) and 6 μ M IC-Green (Akorn Inc. IL) yielding a liquid with $\mu'_s=7 \text{ cm}^{-1}$ and $\mu_a=0.05 \text{ cm}^{-1}$ at 675nm. Two glass tubes (4mm outer - 3.5 mm inner diameter) were inserted with centers 12 mm apart, at different depths as shown in Figure 1. The first tube that traversed the field of view FOV (i.e. the volume reconstructed) contained 500nM of Cy5.5 (Amersham pharmacia biotech NJ) and 0.5% Intralipid and the second tube that was inserted only by 8mm in the FOV contained 750nM of Cy5.5. Cy 5.5 concentrations were verified with a calibrated U3000 Hitachi spectrophotometer. The light source was a 675nm, 2mW continuous wave laser diode (Thorlabs NJ) with 2% amplitude noise. Light was switched sequentially to the 24 source positions using an optical switch (Dicon FiberOptics CA). The light was directed onto the

optical bore using a 200/230 μ m multimode optical fibers (Fiber Instrument Sales NY). For light detection 3mm diameter optical fiber bundles were used (Dollan-Jenner Industries MA) which were imaged on a CCD camera (Roper Scientific NJ) using a Micro-Nikkor f/2.8D AF lens (Nikon JP). For fluorescence detection a three-cavity band-pass filter was used with center frequency at 710nm and 10nm full-width at half maximum (Andover Corporation NH).

Inversion of Eq. 3 after discretization was performed using the algebraic reconstruction technique⁹, which was run until the result showed changes of less than 0.01% per 10 iterations (approximately 3000 iterations run in \sim 5 minutes on a 1GHz Intel Pentium III personal computer). Since the problem is solved at $\omega=0$, only $n(\vec{r})$ was reconstructed. The functions U_0 and G were calculated for the cylindrical boundary using a finite-difference solution of the homogenous diffusion equation for the background medium. A zero-boundary condition¹³ was assumed at $1/\mu_s'$ outside the actual boundary. Three planes were simultaneously reconstructed along the z plane with voxel size $h=0.833 \times 0.12 \times 0.12$ cm³ (total of 1047 voxels).

Figure 2 depicts the reconstructed planes using U_{inc} in Eq.3, which is the incident photon field measured through the homogeneous background solution of IC-Green and Intralipid with no fluorochrome objects immersed. Each plane depicted, is interpolated to a 60x60 grid ($h' = 0.04 \times 0.04$ cm²). Two cylinders appear in the top plane and one cylinder in the middle and lower plane as expected. Quantification was within 10% of the expected Cy5.5 concentration. The size of the cylinder was correctly resolved at the middle plane (within \pm half voxel size) but was overestimated for the top and bottom planes by \sim 30%. This is typical in such reconstructions because the top and bottom planes have virtually half the number of light path-length projections passing through them than the planes in the middle and hence there is less information available for the medium at the top and bottom. To overcome this effect it would be desirable to increase the number of source-detector rings along z so that the field of view is fully contained within the source-detector rings.

Figure 3 depicts the reconstructions obtained when using U'_{inc} in Eq.3, which is the photon field measured at the excitation wavelength with the fluorochrome objects immersed. Although no short-wave-pass filter was used, the influence of emission photons is negligible because $U'_{inc} \gg U_{fl}$. The reconstructed images appear essentially identical to the ones in Figure 2. There were small ($<3\%$) differences in the quantification of objects. The shape of the objects reconstructed also demonstrates minor differences but the center of the objects did not change. Tissue-like background heterogeneity could have a stronger effect in the accuracy of the result. However this effect should be no different than the one seen in clinical applications of DOT for imaging absorption perturbations¹², since absorption DOT uses analogous assumptions¹¹.

In conclusion, we have demonstrated three-dimensional tomographic reconstructions of different fluorochrome concentration in diffuse, tissue-like phantoms using a novel animal imager. These results were obtained using a reconstruction algorithm that is appropriate for clinical measurements since measurement calibration can be performed virtually simultaneously with the fluorescent measurement, hence maintaining high positional accuracy, under the same physiological/biochemical

conditions and maximize patient comfort. The algorithm and described tomographic imaging system should provide a highly useful tool to measure a variety of functional and molecular abnormalities in tissues in-vivo.

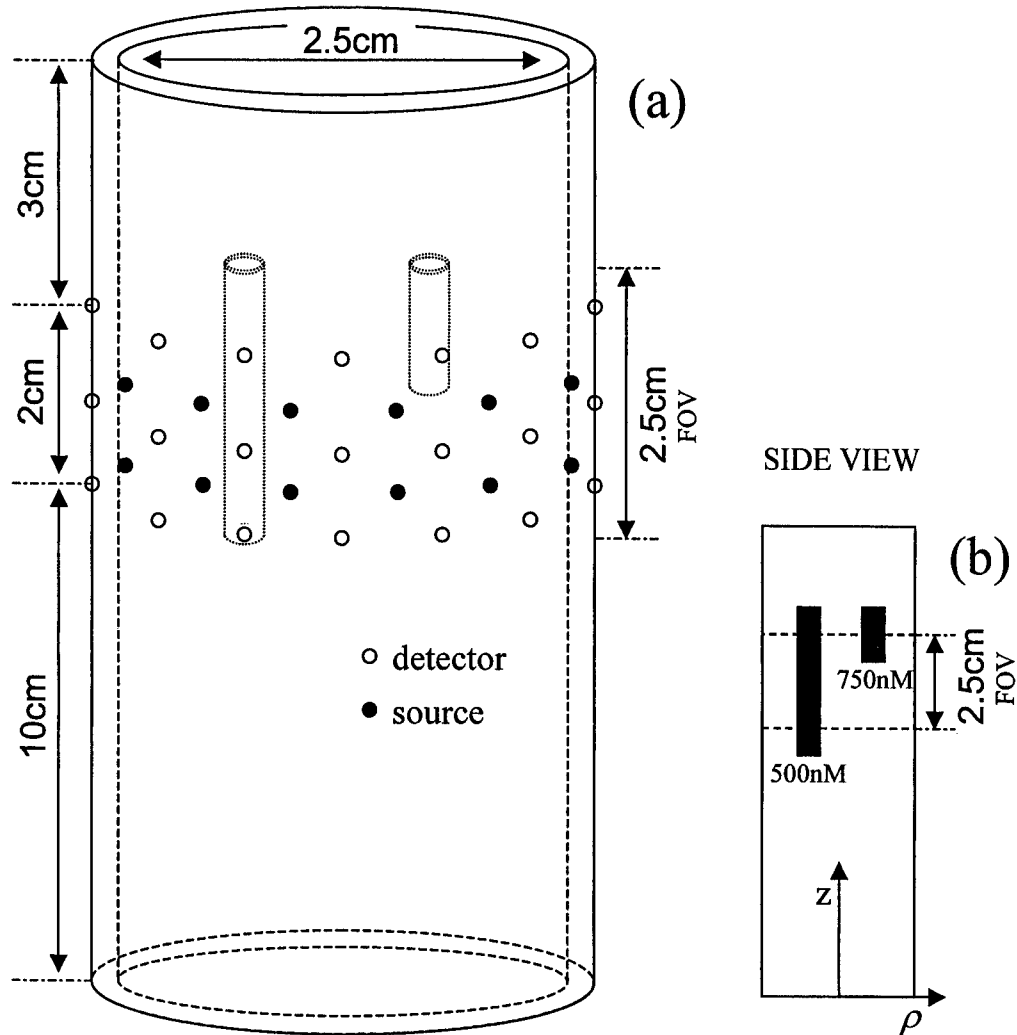


Figure 1. a) Optical bore, made of Delrin® acetal resin. The fibers pass through the Delrin material and come face with the inner walls. The tubes immersed into the intralipid solution are shown in dotted lines. b) Side view of (a).

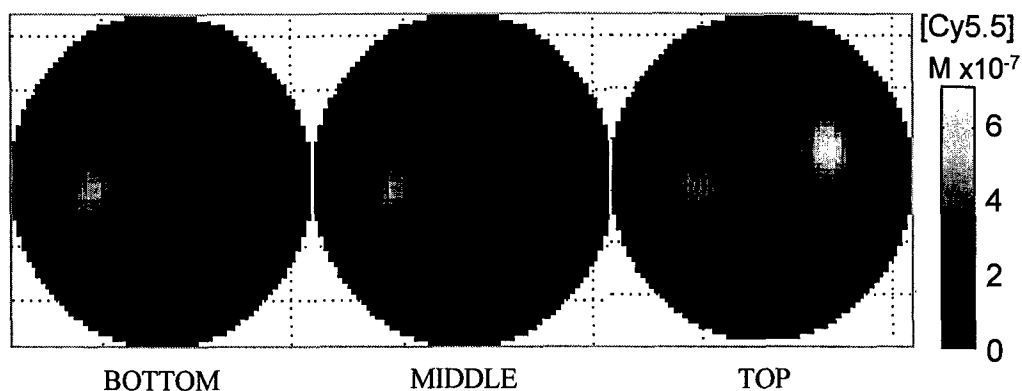


Figure 2. Fluorescence reconstruction of the experimental set-up of Figure 1 using three layers along z . The fluorescence measurements are normalized using U_{inc} i.e. the incident field measured when the two absorbing/fluorescent objects were not immersed.

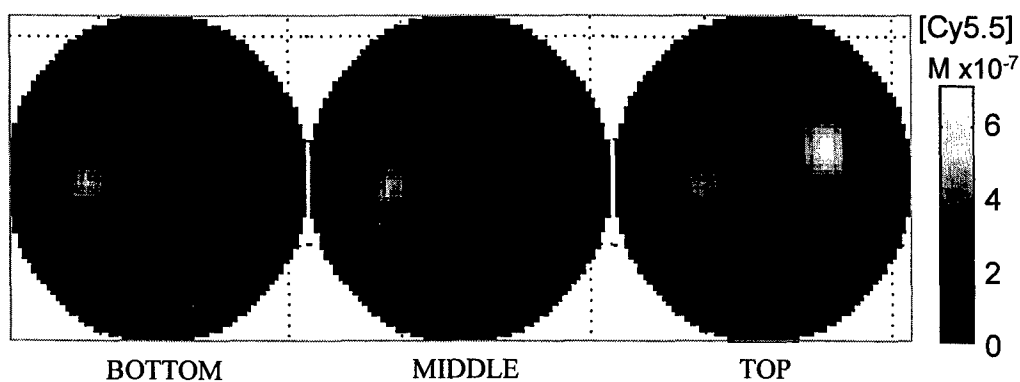


Figure 3. Fluorescence reconstruction of the experimental set-up of Figure 1b using three layers along z . The fluorescence measurements are normalized using U'_{inc} i.e. the incident field measured with the two absorbing/fluorescent objects immersed.

REFERENCES

- ¹ Licha K., Riefke B., Ntziachristos V., Becker A., Chance B., Semmler W. *Photochem. Photobiol.* **72**, 392-398 (2000).
- ² Achilefu, S. Dorshow, R. B. Bugaj, J. E. Rajagopalan, R. *Invest. Radiol.* **35**(8):479-485 (2000).
- ³ Weissleder R., Tung CH., Mahmood U., Bogdanov A. Jr., *Nat. Biotechnology* **17**:375-378 (1999).
- ⁴ D.Y. Paithankar, A.U. Chen, B.W. Pogue, M.S. Patterson, E.M. Sevick-Muraca, *Appl. Opt.* **36**(10):2260-2272 (1997).
- ⁵ H. Jiang, *Appl. Opt.* **37**(22): 5337-5343 (1998)
- ⁶ M.A. O'Leary, D.A. Boas, X.D. Li, B. Chance, A.G. Yodh, *Opt. Lett.* **21**(2): 158-160 (1996).
- ⁷ J.B. Fishkin, E. Gratton, *J. Opt. Soc. Am. A* **10**, 127-140 (1993)
- ⁸ Li XD, OLeary MA, Boas DA, Chance B, Yodh AG. *Appl. Opt.* **35**: (19) 3746-3758 (1996).
- ⁹ A.C. Kak, M. Slaney, "Principles of Computerized Tomographic Imaging", IEEE Press, New York (1988).
- ¹⁰ O'Leary, M.A., Boas, D.A., Chance B. and Yodh, A.G. *Opt. Lett.*, **20**(5), 426-428 (1995).
- ¹¹ V. Ntziachristos, A. Hielscher, A.G. Yodh, B. Chance, submitted to IEEE transactions on Medical Imaging (2000) [In part published at : Ntziachristos V., Hielscher A.H., Yodh A.G., Chance B., in *Biomedical Optics : Advances in Optical Imaging, Photon Migration and Tissue Optics*, OSA Technical Digest CLEO/Europe **AMB3-1** : 211-213, Munich, Germany (1999).]
- ¹² Ntziachristos V., Yodh A.G., Schnall M., Chance B., *Proceedings of the National Academy of Sciences, USA.* **97**: (6) 2767-2772, (2000).
- ¹³ Kienle A., Patterson MSJ. *Opt. Soc. Am. A* **14**(1) 246-254 (1997).

REPORT #3

Fluorescence-mediated tomography resolves protease activity in vivo.

Vasilis Ntziachristos, Ching-Hsuan Tung, Christoph Bremer and Ralph Weissleder

Center for Molecular Imaging Research

**Massachusetts General Hospital & Harvard Medical School.
Charlestown MA 02129**

Abstract

Systematic efforts are under way to develop novel technologies that would allow molecular sensing in intact organisms in vivo. Using inversion techniques that account for the diffuse nature of photon propagation in tissue and near infrared fluorescent molecular beacons we were able to obtain three-dimensional in-vivo images of cathepsin B expression of orthopic gliomas. We demonstrate that activatable fluorochromes can be detected with high positional accuracy in deep tissues, that molecular specificities of different beacons towards enzymes can be resolved, and that tomography of beacon activation is linearly related to enzyme concentration. The tomographic imaging method offers a range of new capabilities for studying biological function using fluorescent chemical sensors, for identifying molecular expression patterns via multispectral imaging and for continuously monitoring drug therapies.

Keywords: molecular sensing, murine models, tomography, imaging, near infrared fluorescence

Main text

Compounds exhibiting fluorescent properties in the visible and near-infrared light range play an important role in many biotechnology applications including gene expression profiling, determining protein function, elucidating cellular pathways, in sensing small molecule protein interaction, or in measuring physiologic solutes¹⁻³. Inducible photoproteins, sensing protein chimera, organic fluorochromes, quantum dots, resonating nanoparticles and lanthanide complexes have thus been used as reporters for probing fluorescence, fluorescence energy transfer (FRET), spectral analysis or fluorescence lifetime (FLT)^{2,4-9}. More recently, near infrared (700-900 nm) targeted fluorochromes, sensing fluorogenic substrates and red-shifted photoproteins with higher tissue penetration have been developed to measure molecular events in vivo in small animals^{10,11}.

Fluorescence generated in in-vitro assays can be easily quantified using fluorometers or charge coupled devices (CCD). Similarly, fluorescence of superficial structures has been imaged in vivo using confocal or multiphoton microscopy¹²⁻¹⁴. Quantitation of fluorescence by imaging and sensing fluorochrome reporters in deep structures (> 1 mm) however, has been more elusive. Here we describe the in-vivo implementation of fluorescence mediated tomography (FMT) to image fluorescence in deeper tissues in murine models and show how highly sensitive measurements with molecular specificity can be obtained. FMT is a novel, quantitative 3D imaging technique capable of sensing pico- to femtomole quantities of fluorochromes in tissues at macroscopic scale, i.e. in whole animals with mm resolution. The technique shares tomographic principles with diffuse optical tomography¹⁵⁻¹⁷ but simultaneously uses absorption and fluorescent measurements for accurate three-dimensional reconstruction of fluorochrome concentration¹⁸.

A tomographic imaging system, shown in Fig. 1, was constructed. Laser light at 670 nm (a), operating in 40 mW continuous mode, was used to successively excite 24 point sources in two 12-fiber layers within the cylindrical imaging chamber (e) (2.5 cm diameter) by using an optical switch (d) (Dicon Fiberoptics CA). For each excitation point, the output of three layers, each of 12 detection fiber bundles (g), was captured onto a 6x6 array (h) (c.f. inset of Fig.1) and imaged using a high quantum yield CCD camera (j) (Roper Scientific NJ). Measurements were acquired for excitation light (absorption and scattering signal), and fluorescence using a band-pass interference filter (i) (Andover Corporation NH) yielding two vectors of 864 data points each. Additional measurements were obtained in a reference channel (c) through a beam-splitter (b) (OZ Optics Ontario Canada) to account for temporal laser fluctuations. For image reconstruction and data processing, the illuminated imaging volume was segmented into 5 layers containing each 491 voxels, the voxel size being $1 \times 1 \times 5 \text{ mm}^3$. For data reconstruction, each voxel was assigned an initially unknown fluorochrome concentration. Then a forward problem was constructed that predicted a synthetic measurement¹⁹, i.e. the ratio of photons detected at the emission wavelength after correction for bleed-through signals over the photons detected at the excitation wavelength for an assumed known fluorescence distribution in the medium¹⁸ (c.f. inset of Fig.1). The forward model was inverted using algebraic reconstruction techniques with positive restriction for the experimentally obtained measurement vector. Reconstructed images display the fluorochrome concentration in nanomolar units, calibrated against free and quenched near infrared indocyanine compounds.

To determine the sensitivity by which measurements could be carried out in turbid media, indocyanine fluorochrome samples (100 μL) were embedded in highly scattering media simulating optical properties of parenchymal tissue. With the current acquisition set-up, the detection threshold of fluorochrome was approximately two hundred femtomoles in the embedded target volume deep in the phantom²⁰. The detection limit is a function of multiple variables including the number of source/detector pairs, imaging time, laser output, CCD characteristics and the optical properties and dimensions of the medium of investigation. With state of the art technology it is estimated that fluorescence detection could be further decreased by at least two orders of magnitude using liquid nitrogen cooled CCD cameras, higher power lasers, more red-shifted fluorochromes and by improving the coupling efficiency of photons onto the CCD chip²¹. In a separate experiment the spatial resolution of the constructed tomographer was also determined by the ability to separate two 1 mm cylinders embedded in fluid simulating optical properties of parenchymal tissue. The spatial resolution of the FMT system, ranged from 1 mm near the surface to approximately 2.5 mm in the center of the volume²⁰. Finally the quantification error has been shown to be within 10% of the expected fluorochrome concentration for the experimental set-up employed¹⁸. Again, increasing the source/detector pairs and power settings could be further used to improve the above resolutions and quantifications by improving the spatial information and signal to noise ratio detected.

The ability to detect fluorochromes *in vivo* would be of considerable biomedical interest, as generic fluorochromes and those targeted to receptors have recently been described^{22,23}. An inherently higher signal-to-noise ratio can be achieved by using activatable fluorochromes ("molecular beacons"), which become fluorescent after hybridization²⁴ or enzymatic cleavage²⁵. We therefore tested whether the tomographic imaging system could resolve the enzyme activity of cathepsin-B in turbid media²⁶, using a previously developed biocompatible NIR cathepsin B sensitive molecular beacon²⁷. The experimental setup, shown in Fig 2a, was such that four capillaries contained 200 μL of a 1 μM cathepsin-B sensitive imaging probe to which was added either 0, 5, 25 or 50 μg of purified cathepsin B (Calbiochem, La Jolla, CA). The capillaries were enclosed in turbid media as shown in Fig. 2a and imaged over time with each acquisition taking 2 minutes. The surrounding turbid media was constructed out of polyester resin (Creative Wholesale Stockbridge GA) to which TiO_2 particles (Sigma St. Louis MI) and India Ink (KOH-I-NOOR Leeds, MA) had been added to simulate tissue scattering and absorption. The reconstructed values shown in Fig. 2b demonstrate a linear relation between enzyme concentration and fluorochrome activation covering a range of physiologically encountered enzyme levels, obtained at 4 and 24 hours after enzyme administration. This result indicates that fluorescence reconstructions could be used for quantitative insights into enzymatic function.

In another set of experiments, we examined whether the tomographic imaging system could resolve specific enzymatic activity when tested with the above described reporter probe. Cathepsin B, D and H were added in different capillaries of the same experimental setup shown in Fig. 2a at 25 μg /capillary diluted in buffer²⁸. All capillaries contained the cathepsin B sensitive NIR fluorescent probe (1 μM). The fourth capillary was in the absence of an enzyme for control purposes. Fig. 2c shows the reconstructed middle slice 24h after substrate/enzyme interaction. Activation of the cathepsin B sensitive probe by cathepsin B is clearly evident, whereas it was lacking for the other cathepsins. The kinetics of probe activation due to cathepsin B versus cathepsin D is shown in Fig 2d. Cathepsin H demonstrated a very similar activation pattern with cathepsin D while the fourth tube

demonstrated minimal background fluorescence. Measurements performed under identical conditions in non-turbid media using a fluorometer (F4500, Hitachi) are plotted on Fig. 2d as triangles and verify the activation rate calculated by FMT. Summarily, the above results show that 1) the technique is specific in differentiating fluorescence activation imparted by different enzymes, that 2) there is a predictable relation between enzyme activity and generated fluorescence under the tested conditions and that 3) measurements obtained by FMT imaging from within turbid media closely reflect those obtained using an analytical fluorometer under non-turbid conditions. It appears, that the technique should thus be able to measure a number of different sensing molecular probes currently under development.

While the above experiments were performed *in vitro* using phantoms and tissue-like turbid media, the main challenge was to determine whether similar experiments could be performed in murine models. As an extension to the above validation studies, we chose to image cathepsin B activity in 9L gliosarcomas stereotactically implanted into unilateral brain hemispheres of nude mice, as cathepsin B activity had been implicated in glioma invasion^{26,29,30}. All animals³¹ were subjected to correlative MR imaging to determine the presence and location of tumors prior to the FMT imaging studies. Fig. 3 summarizes a representative imaging experiment. Fig. 3a-b depict the gadolinium-enhanced tumor (enhancement is shown in a green color map superimposed onto a T1 weighted image) on axial (a) and sagittal (b) slices. Fig. 3c, e and f depict the three consecutive FMT slices obtained from top to bottom of the volume of interest. The location and volume covered by the three slices, is indicated on Fig. 3b by thin white horizontal lines. Fig. 3c shows marked local probe activation relative to adjacent slices, congruent with the location of the tumor identified on the MR images. Fig. 3d shows a superposition of the MR axial slice passing through the tumor (Fig. 3a) onto the corresponding FMT slice (Fig. 3c) after appropriately translating the MR image to the actual dimensions of the FMT image. For coregistration purposes we used special water-containing fiducials and body marks that facilitated matching of the MR and FMT orientation and animal positioning. The *in-vivo* imaging data correlated well with surface weighted reflectance imaging of the excised brain. Fig. 3g depicts the axial brain section through the 9L tumor examined with white light using a CCD camera mounted onto a dissecting microscope, Fig. 3h shows the same brain section imaged using a previously developed reflectance imaging system³² at the excitation wavelength (675 nm) and Fig. 3i is the fluorescence image obtained at the emission wavelength using appropriate 3-cavity cut-off filters (Andover Corporation NH) that demonstrates a marked fluorescent probe activation, congruent with the tumor position identified by gadolinium-enhanced MRI and FMT. On average, the concentration of activated fluorochrome per tumor, as calculated by FMT was about 110 ± 30 nM. The above results, confirm that cathepsin B can be used as an imaging marker²⁷ since the protease is produced in considerable amounts by tumor cells and recruited host cells³³. Cathepsin B expression in the tumors was further confirmed by immunohistochemistry, Western blotting and RT-PCR (data not shown).

To study whether FMT imaging could reveal different levels of cathepsin B enzyme expression we also performed correlative imaging and analysis in another tumor model (HT1080) known to have higher levels of a number of different proteases^{25,34}. Using the same imaging set-up described above we determined a 5 fold higher cathepsin B activity in size matched HT1080 tumors (a human fibrosarcoma) compared to 9L tumors. These results were confirmed by RT-PCR and western blotting, the latter revealing 4 fold higher cathepsin B protein levels in HT1080 tumors compared to 9L tumors. Similar results were also observed in other models in which HT1080 tumors had been implanted into the lung or

retroperitoneum or when transgenic animals developing breast tumors were used (data not shown). FMT imaging thus offers the potential for investigating enzyme specific events in live animals, opening unique opportunities for sensing a wider array of enzymes. While the current studies only used cathepsin B as a marker for consistency, many other proteases could potentially be revealed in vivo. In more recent experiments biocompatible imaging probes have been synthesized for cathepsin D³⁵, cathepsin K, MMP-2²⁵ among others. The number of known proteases is increasing at a tremendous rate as a consequence of genome sequencing projects. Through sequence homology to known proteases, and other high throughput tools³⁶, it should be possible to find unique peptide substrates with high specificity for given enzymes. Furthermore, larger numbers of affinity molecules, derived from high throughput screens³⁷ could be tagged with fluorochromes and be rapidly screened in mouse models. Such "in vivo assays" could become powerful adjuncts to drug development as they take into account physiology and disease-host interactions. With image acquisition times of only a few minutes (typically two to three minutes in the animals studied), FMT imaging has considerable advantages over existing technologies in providing high throughput functional information in intact living animals.

How can the technology be adapted clinically? NIR light has been shown to penetrate tissues several centimeters and detection is thus not necessarily limited to small volumes. Indeed, recent measurements and modeling²¹ show that near infrared fluorescent signals from tumor-like structures can propagate for more than 15 centimeters in breast or lung tissue and more than 5 cm in the adult brain. Again, these estimates may well be surpassed by newer detection technologies and/or more efficient beacons. While we chose to construct a cylindrical imaging chamber for mice, human imaging systems could well have different geometries for more efficient light collection. Planar imaging geometries, handheld scanners or even endoscopic sensors are all technologically feasible providing optimized approaches for imaging of specific organs or diseases. An important aspect to potential clinical tomographic imaging is the fact that FMT is inherently quantitative and can be acquired over time for monitoring purposes. Additional advantages include the fact that no radiation is required, that beacons and fluorochromes are usually stable and do not decay like isotopes and that the technology is relatively inexpensive compared to other tomographic imaging systems. It is also conceivable to perform multi-wavelength imaging to obtain information from multiple targets or to validate measurements similar as in comparative hybridization experiments. The former is of particular clinical relevance as "expression patterns" rather than single molecules may form the basis for more sophisticated future imaging techniques. Finally, FMT imaging should be useful for monitoring drug therapies at the molecular levels²⁵ over time and in tailoring treatments in individual patients. FMT imaging may also be a useful adjunct to x-ray computed tomography and magnetic resonance imaging. It is thus hoped that FMT imaging will find applications in unraveling complex biological pathways in murine models and in applying this knowledge to current problem areas in clinical diagnosis and drug testing.

FIGURES

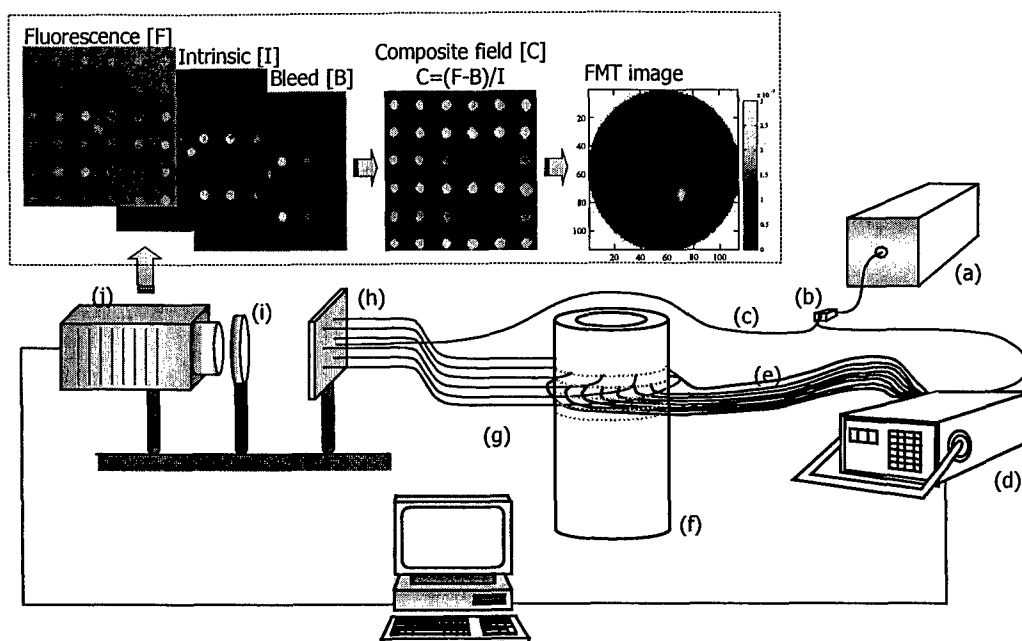


Figure 1. Schematic of the FMT imager used for the experimental measurements. The insert surrounded by the dotted line describes the typical measurements and formation of the composite measurement, necessary to produce quantified images (for details see text).

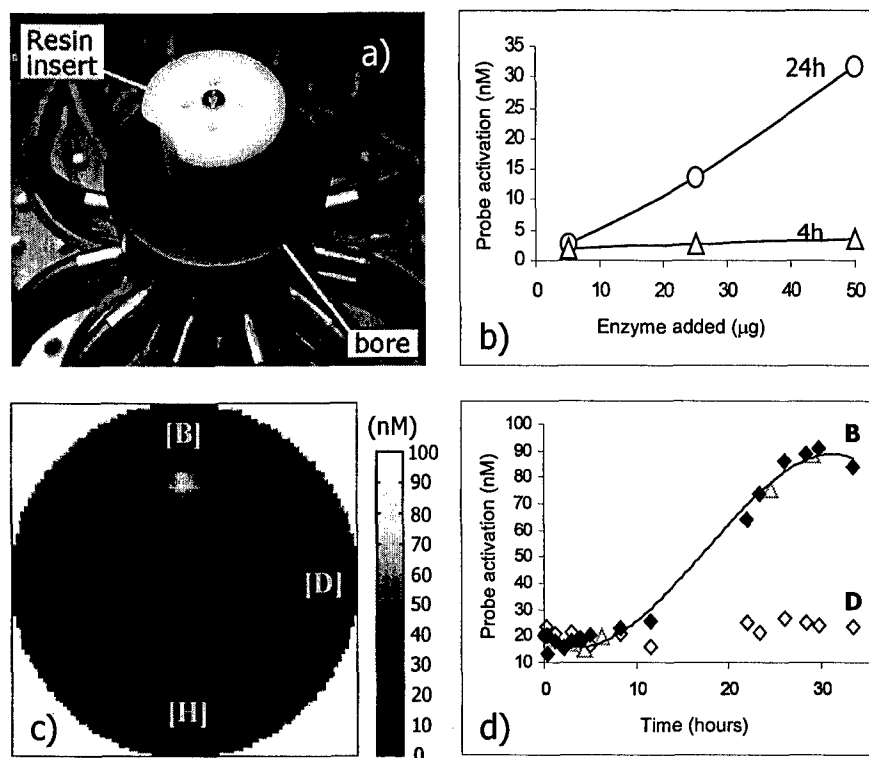


Figure 2. **a)** Photograph of the turbid resin tube (shown inserted into the optical chamber), used for two in-vitro experiments summarized here. The four capillaries shown were filled with $1\mu\text{M}$ of a cathepsin-B sensitive NIR activatable probe for both experiments. **b)** (Experiment 1): Probe activation as a function of cathepsin B concentration obtained with FMT at 4 and 24 hours after enzyme addition. **c)** (Experiment 2): FMT reconstruction obtained from the middle slice of the resin tube at 24h after 25 μg of cathepsins (B, D, H) were added in different capillaries as marked on the image. The fourth capillary did not contain any enzyme. **d)** (Experiment 2 cont.): Activation kinetics obtained with FMT from the capillaries containing cathepsin B and D. The orange triangles indicate measurements obtained in parallel with a fluorometer in the absence of the turbid medium.

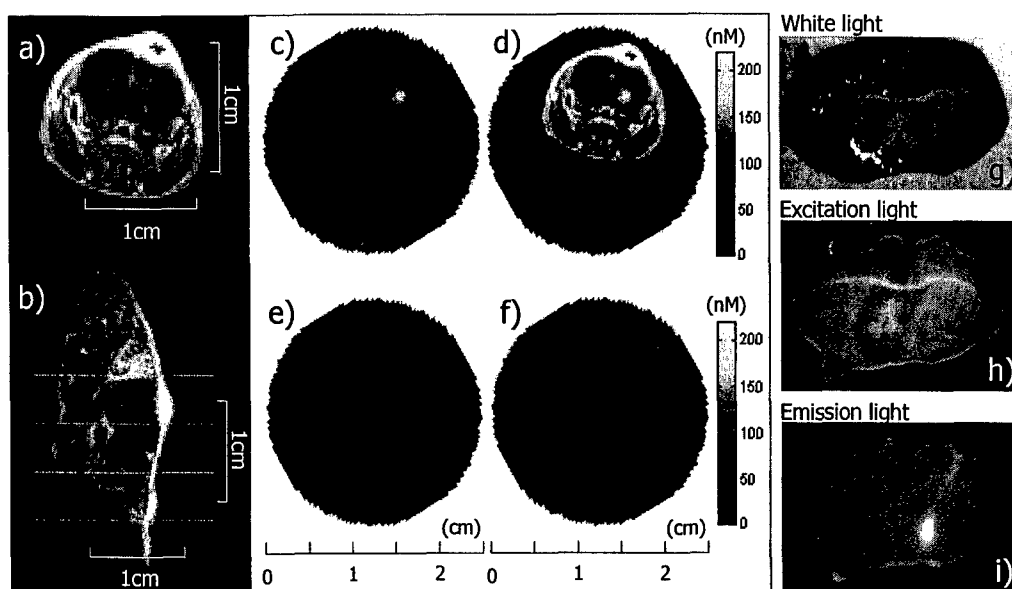


Figure 3. In-vivo FMT of cathepsin B expression levels in 9L gliosarcomas stereotactically implanted into unilateral brain hemispheres of nude mice. **a), b)** Axial and sagittal MR slices of an animal implanted with a tumor, which is shown in green after gadolinium enhancement. **c), e), f),** Consecutive FMT slices obtained from top to bottom from the volume of interest shown on (b) by thin white horizontal lines. **d)** Superposition of the MR axial slice passing through the tumor (a) onto the corresponding FMT slice (c) after appropriately translating the MR image to the actual dimensions of the FMT image. **g), h)** Axial brain section through the 9L tumor imaged with white light and with monochromatic light at the excitation wavelength (675 nm) respectively, and **i)** fluorescence image of the same axial brain section demonstrating a marked fluorescent probe activation, congruent with the tumor position identified by gadolinium-enhanced MRI and FMT.

REFERENCES

1. Emmert-Buck, M. R. et al. Molecular profiling of clinical tissue specimens: feasibility and applications. *Am J Pathol* **156**, 1109-15. (2000).
2. Ando, H., Furuta, T., Tsien, R. & Okamoto, H. Photo-mediated gene activation using caged RNA/DNA in zebrafish embryos. *Nature Genetics* **28**, 317-25 (2001).
3. Wouters, F. S., Verveer, P. J. & Bastiaens, P. I. Imaging biochemistry inside cells. *Trends in Cell Biology* **11**, 203-11 (2001).
4. Han, M., Gao, X., Su, J. Z. & Nie, S. Quantum-dot-tagged microbeads for multiplexed optical coding of biomolecules. *Nat Biotechnol* **19**, 631-5. (2001).
5. Georgakoudi, I. et al. Fluorescence, reflectance, and light-scattering spectroscopy for evaluating dysplasia in patients with Barrett's esophagus. *Gastroenterology* **120**, 1620-1629 (2001).
6. Pollok, B. A. & Heim, R. Using GFP in FRET-based applications. *Trends in Cell Biology* **9**, 57-60 (1999).
7. Bastiaens, P. I. & Squire, A. Fluorescence lifetime imaging microscopy: spatial resolution of biochemical processes in the cell. *Trends in Cell Biology* **9**, 48-52 (1999).
8. Pepperkok, R., Squire, A., Geley, S. & Bastiaens, P. I. H. Simultaneous detection of multiple green fluorescent proteins in live cells by fluorescence lifetime imaging microscopy. *Current Biology* **9**, 269-272 (1999).
9. Fukumura, D. et al. Tumor induction of VEGF promoter activity in stromal cells. *Cell* **94**, 715-25. (1998).
10. Weissleder, R. A clearer vision for in vivo imaging. *Nature Biotech* **19**, 316-317 (2001).
11. Gross, L. A., Baird, G. S., Hoffman, R. C., Baldrige, K. K. & Tsien, R. Y. The structure of the chromophore within DsRed, a red fluorescent protein from coral. *Proc Natl Acad Sci U S A* **97**, 11990-5. (2000).
12. Bacskai, B. J. et al. Imaging of amyloid-beta deposits in brains of living mice permits direct observation of clearance of plaques with immunotherapy. *Nature Medicine* **7**, 369-72 (2001).
13. Brown, E. B. et al. In vivo measurement of gene expression, angiogenesis and physiological function in tumors using multiphoton laser scanning microscopy. *Nat Med* **7**, 864-8. (2001).
14. Tsien, R. Y. & Miyawaki, A. Seeing the machinery of live cells. *Science* **280**, 1954-5. (1998).
15. Yodh, A. G. & Chance, B. Spectroscopy and Imaging with Diffusing Light. *Physics Today* **48**, 34-40 (1995).
16. Arridge, S. Optical tomography in medical imaging. *Inverse Problems* **15**, R41-R93 (1999).
17. Ntziachristos, V., Yodh, A. G., Schnall, M. & Chance, B. Concurrent MRI and diffuse optical tomography of breast after indocyanine green enhancement. *Proceedings of the National Academy of Sciences of the United States of America* **97**, 2767-2772 (2000).
18. Ntziachristos, V. & Weissleder, R. Experimental three-dimensional fluorescence reconstruction of diffuse media using a normalized Born approximation. *Optics Letters* **26**, 893-895 (2001).

19. The exact form of the synthetic measurement $U_f(\vec{r}_s, \vec{r}_d)$ detected at position \vec{r}_d due to a source at position \vec{r}_s , and its relation to the fluorescent distribution in the tissue of investigation can be written as

$$U(\vec{r}_s, \vec{r}_d) = S_0 \cdot \frac{U_f(\vec{r}_s, \vec{r}_d) - U_{bl}(\vec{r}_s, \vec{r}_d)}{U_{inc}(\vec{r}_s, \vec{r}_d)} = \frac{1}{U_0(\vec{r}_s, \vec{r}_d, k^{\lambda_1})} \cdot \int d^3 r \cdot (U_0(\vec{r}_s - \vec{r}, k^{\lambda_1}) n(\vec{r}) \frac{\nu}{D^{\lambda_2}} G(\vec{r}_d - \vec{r}, k^{\lambda_2}))$$

where $U_f(\vec{r}_s, \vec{r}_d)$, $U_{inc}(\vec{r}_s, \vec{r}_d)$ are measurements at the emission and excitation wavelength respectively, $U_{bl}(\vec{r}_s, \vec{r}_d) = \Theta_f \cdot U_{inc}(\vec{r}_s, \vec{r}_d)$ is the bleed through signal, Θ_f is the band-pass filter attenuation factor, S_0 is a gain term that accounts for instrument gain differences at the excitation (λ_1) and emission (λ_2) wavelengths, $n(\vec{r})$ is the product of the fluorochrome absorption coefficient and fluorescence quantum yield, $k^{\lambda_1}, k^{\lambda_2}$ are the wave propagation vectors at λ_1 and λ_2 respectively, ν is the speed of light into the medium, D^{λ_2} is the diffusion coefficient at the λ_2 , $U_0(\vec{r}_s - \vec{r}, k^{\lambda_1})$ is a term that describes the established photon field at position \vec{r} into the medium at λ_1 and $G(\vec{r}_d - \vec{r}, k^{\lambda_2})$ is a term that describes the propagation of the emission photon wave from a fluorochrome at position \vec{r} to the detector.

20. Ntziachristos, V. & Weissleder, R. CCD-based scanner for three-dimensional fluorescence-mediated diffuse optical tomography of small animals. *submitted Medical Physics* (2001).
21. Ntziachristos, V., Ripoll J. & Weissleder, R. Would near-infrared fluorescence signals propagate through large human organs for clinical studies? *Opt Lett submitted* (2001).
22. Becker, A. et al. Receptor targeted optical imaging of tumors with near infrared fluorescent ligands. *Nature Biotech*, page number in the same issue (2001).
23. Achilefu, S., Dorshow, R. B., Bugaj, J. E. & Rajagopalan, R. Novel receptor-targeted fluorescent contrast agents for in vivo tumor imaging. *Invest Radiol* **35**, 479-85. (2000).
24. Tyagi, S. & Kramer, F. R. Molecular beacons: probes that fluoresce upon hybridization. *Nat Biotechnol* **14**, 303-8. (1996).
25. Bremer, C., Tung, C. & Weissleder, R. Imaging of metalloproteinase2 inhibition in vivo. *Nature Med* **7**, 743-748 (2001).
26. Demchik, L. L., Sameni, M., Nelson, K., Mikkelsen, T. & Sloane, B. F. Cathepsin B and glioma invasion. *Int J Dev Neurosci* **17**, 483-94 (1999).
27. Weissleder, R., Tung, C. H., Mahmood, U. & Bogdanov, A., Jr. In vivo imaging of tumors with protease-activated near-infrared fluorescent probes. *Nat Biotechnol* **17**, 375-8 (1999).
28. The buffers used for cathepsin B, D and H were sodium phosphate 0.1M, pH 6.0, 1mM DTT; 50mM Glycine/HCl, pH 3.5 and 750mM sodium phosphate pH 6.8, 1mM EDTA, 3mM cysteine, respectively.
29. Yan, S., Sameni, M. & Sloane, B. F. Cathepsin B and human tumor progression. *Biol Chem* **379**, 113-23 (1998).
30. Rempel, S. A. et al. Cathepsin B expression and localization in glioma progression and invasion. *Cancer Res* **54**, 6027-31 (1994).

31. A total of seven animals with 9L implanted tumors and five animals with HT1080 tumors implanted in the brain, lung and retroperitoneum were studied.
32. Mahmood, U., Tung, C. H., Bogdanov, A., Jr. & Weissleder, R. Near-infrared optical imaging of protease activity for tumor detection. *Radiology* **213**, 866-70 (1999).
33. Koblinski, J. E., Ahram, M. & Sloane, B. F. Unraveling the role of proteases in cancer. *Clin Chim Acta* **291**, 113-35. (2000).
34. Giambernardi, T. A. et al. Overview of matrix metalloproteinase expression in cultured human cells. *Matrix Biol* **16**, 483-96 (1998).
35. Tung, C., Mahmood, U., Bredow, S. & Weissleder, R. In vivo imaging of proteolytic enzyme activity using a novel molecular reporter. *Cancer Research* **in press** (2000).
36. Turk, B. E., Huang, L. L., Piro, E. T. & Cantley, L. C. Determination of protease cleavage site motifs using mixture-based oriented peptide libraries. *Nat Biotechnol* **19**, 661-7. (2001).
37. MacBeath, G. & Schreiber, S. L. Printing proteins as microarrays for high-throughput function determination. *Science* **289**, 1760-3. (2000).



DEPARTMENT OF THE ARMY

US ARMY MEDICAL RESEARCH AND MATERIEL COMMAND
504 SCOTT STREET
FORT DETRICK, MARYLAND 21702-5012

REPLY TO
ATTENTION OF:

MCMR-RMI-S (70-1y)

28 Aug 02

MEMORANDUM FOR Administrator, Defense Technical Information
Center (DTIC-OCA), 8725 John J. Kingman Road, Fort Belvoir,
VA 22060-6218


SUBJECT: Request Change in Distribution Statement

1. The U.S. Army Medical Research and Materiel Command has reexamined the need for the limitation assigned to technical reports written for this Command. Request the limited distribution statement for the enclosed accession numbers be changed to "Approved for public release; distribution unlimited." These reports should be released to the National Technical Information Service.

2. Point of contact for this request is Ms. Kristin Morrow at DSN 343-7327 or by e-mail at Kristin.Morrow@det.amedd.army.mil.

FOR THE COMMANDER:

Encl


PHYLIS M. RINEHART
Deputy Chief of Staff for
Information Management

ADB231838
ADB240253
ADB251610
ADB275099
ADB253637
ADB261538
ADB275186
ADB264648
ADB275102
ADB241899
ADB259033
ADB266113
ADB275663
ADB254489
ADB262700
ADB276708
ADB274345
ADB274844
ADB275154
ADB275535
ADB275101
ADB275451
ADB274597
ADB273871
ADB275145
ADB274505
ADB275851
ADB274459
ADB277942
ADB277404
ADB277494
ADB277536